Resonant X-ray Scattering in 3*d* Electron Systems

Hironori Nakao

1 Introduction

The resonant X-ray scattering (RXS) technique had been used to study local symmetry around the target ion using the anisotropy of the anomalous scattering factor of the atomic scattering factor (ASF) near the absorption energy [1–4]. In 1998, Murakami et al. applied the RXS technique to study orbital and charge ordering. The e_g orbital ordering of Mn^{3+} and the charge ordering of Mn ions in $La_{0.5}Sr_{1.5}MnO_3$ were determined [5]. In the case of $LaMnO_3$, the e_g orbital ordering of Mn^{3+} was clearly determined, and a scattering mechanism was proposed [6]. These results demonstrated the potential for measuring the order parameter of the ordered state. These charge- and orbital-ordered states are important parameters for understanding the origin of various intriguing physical properties in strongly correlated electron systems (SCES) [7, 8]. As a result, RXS studies have been extended to many types of materials [9, 10]. The charge and orbital states of e_g electrons have been systematically studied in manganites [11–19] and thin films [20–24]. Orbital and charge ordering of the t_{2g} electron system has been studied in titanates [25–29] and vanadates [30–38]. Moreover, orbital and charge ordering has been investigated in Fe [39–46], Co [47–50], Ni [51–53], and Cu [54–56] systems.

Historical RXS investigations of manganites are detailed in Chap. 1. Herein, we review studies of orbital ordering in perovskite-type titanate as a typical example. First, we summarize the theoretical framework of RXS in Sect. 2. Next, in Sect. 3, we explain in detail the RXS studies of titanates and discuss the origin of RXS signals. Then, we establish RXS as a technique to determine orbital and charge ordering. Thereafter, we investigate the RXS technique experimentally under extreme conditions; experimental examples are presented in Sect. 4.

H. Nakao (✉)
Condensed Matter Research Center and Photon Factory, IMSS, KEK,
Tsukuba, Ibaraki 305-0801, Japan
e-mail: hironori.nakao@kek.jp

Y. Murakami and S. Ishihara (eds.), *Resonant X-Ray Scattering in Correlated Systems*, Springer Tracts in Modern Physics 269,
DOI 10.1007/978-3-662-53227-0_2

2 Theoretical Framework

The scattering intensity $I(E, \mathbf{Q})$ of X-ray diffraction is proportional to the square of the structure factor $F(E, \mathbf{Q})$:

$$I(E, \mathbf{Q}) = |F(E, \mathbf{Q})|^2 L(E, \mathbf{Q}), \tag{1}$$

where $L(E, \mathbf{Q})$ is a correction term, including the Lorentz factor and sample absorption effect. The structure factor is expressed as

$$F(E, \mathbf{Q}) = \sum_j f_j(E, \mathbf{Q}) \exp(-i\mathbf{Q} \cdot \mathbf{r}_j). \tag{2}$$

$f_j(E, \mathbf{Q})$ is the ASF of the j-th atom at position $\mathbf{r}_j$ in a unit cell. The ASF $f(E, \mathbf{Q})$ is given by

$$f(E, \mathbf{Q}) = f_0(\mathbf{Q}) + f'(E) + if''(E), \tag{3}$$

where $f_0(\mathbf{Q})$ is the Thomson scattering factor and $f'(E)$ and $f''(E)$ are real and imaginary terms of the anomalous scattering factor, respectively. The anomalous scattering factor changes remarkably near the absorption-edge energy E_a. Hence, we can obtain structural and electronic information of only a target ion using the energy dependence of $I(E, \mathbf{Q})$ near E_a.

2.1 Anomalous Scattering Factor: Valence State

The absorption-edge energy, E_a, is quite sensitive to the valence of an adsorbed ion. An energy shift due to valence difference is the so-called *chemical shift*. An RXS signal reflecting charge ordering can be observed only near E_a according to the following explanation. Hence, RXS is a powerful technique for determining the charge-ordering structure.

To calculate the structure factor using Eq. (2), we need the ASF and atomic position, $\mathbf{r}$, of all atoms in a unit cell. The value of the Thomson scattering factor is known, and we can use tabulated ASF values, except near the E_a [57–59]. Therefore, the ASFs, $f'(E)$ and $f''(E)$, of charge-ordered ions are needed to calculate the structure factor of the charge-ordering state.

The imaginary term of the ASF $f''(E)$ can be directly obtained from the absorption coefficient $\mu(E)$ using the following equation.

$$f''(E) = \frac{m_e E}{2Nhe^2} \mu(E), \tag{4}$$

where m_e is the electron mass, e is the electron charge, N is the atomic number density, and h is Planck's constant [57, 60]. The real term of the ASF $f'(E)$ can be calculated using Kramers–Krönig transformation of $f''(E)$:

$$f'(E) = \frac{2}{\pi} P \int_0^\infty \frac{E' f''(E')}{E^2 - E'^2} dE', \tag{5}$$

$$f''(E) = \frac{2E}{\pi} P \int_0^\infty \frac{f'(E')}{E^2 - E'^2} dE'. \tag{6}$$

Next, we present an example to determine the ASF of V ions in vanadium compounds [31]. Here, NaV_2O_5 has an average valence of $V^{4.5+}$ at room temperature, and charge-ordering transitions of V^{4+} and V^{5+} occur at approximately 35 K. To determine the charge-ordering structure, the ASFs of V^{4+} and V^{5+} were estimated using CaV_2O_5 and V_2O_5, which have the same crystal structure as NaV_2O_5 and contain only V^{4+} and V^{5+} ions, respectively. The absorption spectra of the vanadium compounds were obtained, as shown in Fig. 1. The absorption spectrum and absorption coefficient are expressed as follows:

$$I(E) = I_0(E) \exp(-\mu(E)t), \tag{7}$$

$$\mu(E)t = log(I_0(E)/I(E)), \tag{8}$$

where $I_0(E)$ and t are the intensity of incident x-rays and the sample thickness, respectively. E_a of V_2O_5 (V^{5+}) is approximately 1.8 eV higher than that of CaV_2O_5 (V^{4+}), i.e., the chemical shift. The peak at around 5.47 keV is the pre-edge $1s \rightarrow 3d$ transition energy, which is strongly observed as a dipole transition owing to the lack of local inversion symmetry at a vanadium site [61]. A similar feature was observed in the V_2O_3 system [30]. E_a of NaV_2O_5 is placed between the E_a of V_2O_5 and CaV_2O_5,

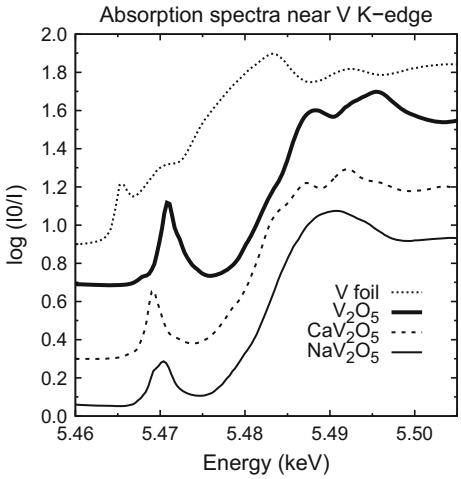

Fig. 1 Absorption spectra of V foil (*dotted line*) and powdered samples of CaV_2O_5 (V^{4+}) (*broken line*), V_2O_5 (V^{5+}) (*thick solid line*), and NaV_2O_5 (*thin solid line*). NaV_2O_5 has an average valence of $V^{4.5+}$ at room temperature, and it shows a charge-ordering transition of V^{4+} and V^{5+} at about 35 K. Part of data were taken from Ref. [31]

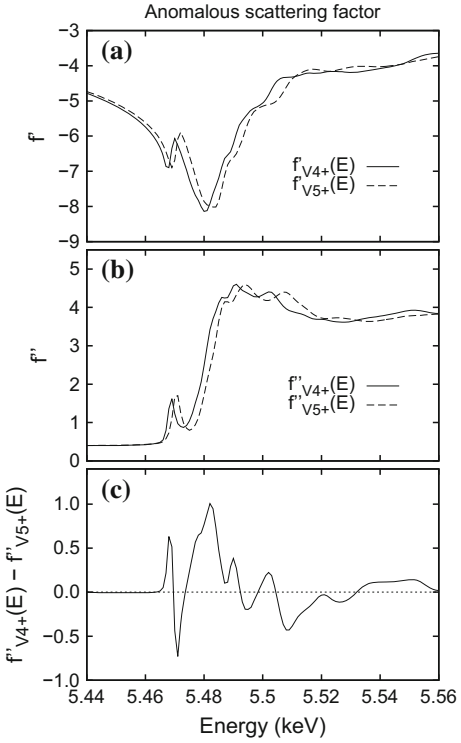

Fig. 2 Energy dependence of ASFs **a** $f'(E)$ and **b** $f''(E)$ for V^{4+} and V^{5+} shown by *solid* and *broken lines*, respectively. **c** Difference between ASFs of V^{4+} and V^{5+}, $f''_{V4+}(E) - f''_{V5+}(E)$. Data were taken from Ref. [31]

and the pre-edge peak broadens, reflecting the existence of V^{4+} and V^{5+}. In contrast, E_a of V foil is considerably lower than those of other compounds. The imaginary parts of the ASFs, $f''(E)$, of V^{4+} and V^{5+} are calculated according to Eq. 4 using $\mu(E)$ of CaV_2O_5 and V_2O_5. Then, $f'(E)$ of V^{4+} and V^{5+} are calculated according to the Kramers–Krönig transformation of $f''(E)$ using the program DIFFKK [60]. The obtained ASFs $f'(E)$ and $f''(E)$ of V^{4+} and V^{5+} are shown in Fig. 2a, b, respectively. The difference between the ASFs of V^{4+} and V^{5+} is small at $E \ll E_a$, whereas it is critically enhanced with a large modulation at E_a. Hence, the difference of one electron between the V^{4+} and V^{5+} sites can be easily detected as the RXS signal $I(E, \mathbf{Q})$, which remarkably changes at E_a. In fact, the charge-ordered state in NaV_2O_5 was clarified using the RXS technique [31, 33].

2.2 *Anomalous Scattering Factor: Orbital State*

Reflecting the anisotropy of orbitals, the ASF becomes a tensor near the absorption energy. This acts as the origin of an RXS signal in orbital-ordering systems. As a result, the RXS intensity indicates a unique azimuthal angle and polarization dependence, which is caused by the tensorized ASF, whereas the usual Thomson scattering

shows no such dependence. In studies of orbital ordering in 3*d* electron systems, RXS at the main edge is mainly used; the $1s \rightarrow 4p$ transition at the main edge is a dipole process. The $4p$ energy level splits because of 3*d* orbital ordering. Then, the ASF becomes a tensor that reflects the anisotropic $4p$ orbital. Two possible scenarios for this lifting have been proposed. One is on-site Coulomb interaction between the $4p$ and 3*d* orbitals, which raises the $4p$ energy level lying parallel to the direction of the extension of the 3*d* orbital (Coulomb mechanism) [63–65]. The other is the anisotropic hybridization of the $4p$ orbital with the p orbital of neighboring ions due to the so-called Jahn–Teller distortion (JTD) (JT mechanism) [66–68]. The origin of $4p$ energy-level splitting depends on the type of system, and it remains controversial as to which of the mechanisms is more significant from the viewpoint of giving rise to RXS [69]. Here, we consider the $3x^2 - r^2$ orbital, as shown in Fig. 3b. In the case of the Coulomb mechanism, $4p$ energy levels are split by on-site Coulomb interaction. Hence, the $4p_x$ energy level is raised, and the $4p_{y,z}$ energy level is lowered. In contrast, in the case of the JT mechanism, the local structure (octahedron) is distorted, reflecting the anisotropic 3*d* orbital, i.e., the JTD. The octahedron is extended along the x direction. Therefore, the $4p_x$ energy level is lowered, and the $4p_{y,z}$ energy level is raised, as shown in Fig. 3c. However, in both cases, an RXS signal provides information about orbital ordering, and the tensor is described as follows:

$$\hat{f} = \begin{pmatrix} f_{\parallel}(E) & 0 & 0 \\ 0 & f_{\perp}(E) & 0 \\ 0 & 0 & f_{\perp}(E) \end{pmatrix}, \tag{9}$$

where $f_{\parallel}(E)$ ($f_{\perp}(E)$) corresponds to the ASF when the polarization of the incident X-ray $\hat{\varepsilon}_i$ is parallel to the x (y, z) direction. As explained here, the tensor has energy

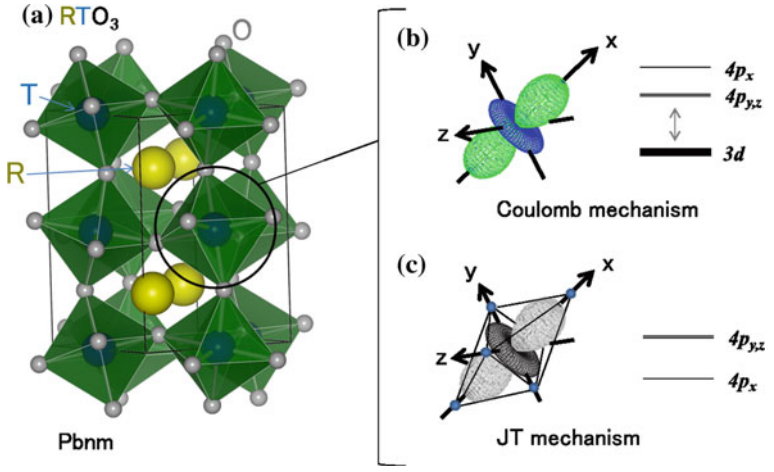

Fig. 3 **a** Perovskite structure with space group *Pbmn*, so called $GdFeO_3$-type structure. **b**, **c** $3x^2 - r^2$ of 3*d* electron orbital. Schematic energy level diagram of $4p_{x,y,z}$ states, which depend on the scenario for the lifting of the degeneracy of $4p$ orbitals

dependence but no Q dependence because the transition is a dipole process. In contrast, the RXS signal at the pre-edge contains the quadrupole transition process, which is the $1s \rightarrow 3d$ transition. In this case, the tensor has Q dependence. The scattering framework is explained in depth in previous studies [10, 62].

Here, we consider the tensor of the structure factor of RTO_3 (T: transition metal with orbital degree of freedom, R: rare earth or Y) perovskite structure with the space group $Pbnm$, as shown in Fig. 3a. There are four T ion sites in the unit cell. The structure factor is expressed by

$$F(E, \mathbf{Q}) = \sum_{j}^{4} \hat{\varepsilon}_i \hat{f}_j(E) \hat{\varepsilon}_s exp(-i\mathbf{Q} \cdot \mathbf{r}_j) + F_o, \tag{10}$$

where $\hat{\varepsilon}_s$ is the polarization vector of the scattered X-ray and F_o is the scalar component of the structure factor. F_o includes the components of R, O atoms and the Thomson scattering factor of T atoms. The tensor in Eq. (9) is defined using xyz coordinates, where the principal axes are aligned with the oxygen direction in the TO_6 octahedron. There is a tilt of the octahedron in the crystal structure with $Pbnm$ ($GdFeO_3$-type structure), as shown in Fig. 3. Hence, the xyz coordination of the tensor depends on T-ion sites. The coordination of the tensor $\hat{f}_j(E)$ is adjusted for calculation using a rotation matrix. On the basis of the structure factor (Eq. (10)), the azimuthal angle dependence of RXS was calculated for titanate and vanadate systems [25, 32, 36].

Let us consider the RXS experimental geometry shown in Fig. 4. The scattering plane defined by $\mathbf{k}_i$ and $\mathbf{k}_f$ is the vertical plane, i.e., the yz plane, where $\mathbf{k}_i$ and $\mathbf{k}_f$ are the wave vectors of incident and scattered X-rays, respectively. The scattering

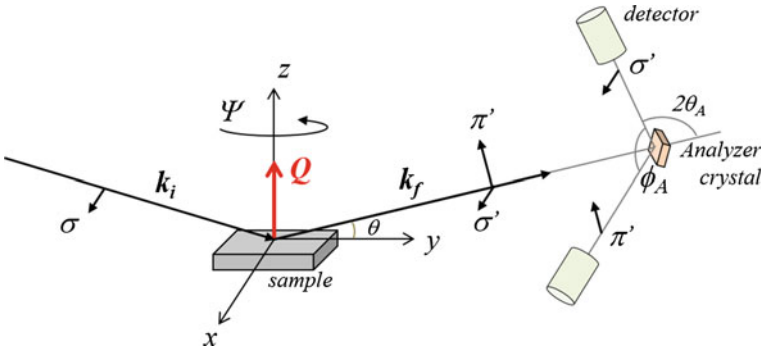

Fig. 4 Schematic geometry of RXS measurement. The scattering plane defined by $\mathbf{k}_i$ and $\mathbf{k}_f$ is vertical, and the scattering vector $\mathbf{Q} = \mathbf{k}_i - \mathbf{k}_f$ is perpendicular to the sample surface in this example, where $\mathbf{k}_i$ and $\mathbf{k}_f$ are the wave vectors of the incident and scattered X-rays, respectively. X-ray polarization is denoted as σ, and π; σ (π) is perpendicular (parallel) to the scattering plane; $\sigma = \sigma' = (1, 0, 0)$ and $\pi' = (0, -\sin\theta, \cos\theta)$. X-ray polarization is analyzed by rotating an analyzer crystal through angle ϕ_A, and $2\theta_A$ is the scattering angle

vector $\mathbf{Q} = \mathbf{k}_i - \mathbf{k}_f$ is perpendicular to the sample surface in this example. The azimuthal angle Ψ, i.e., the angle corresponding to a rotation around the scattering vector $\mathbf{Q}$, is defined as the angle between the scattering plane and reference vector. The incident polarization vector is denoted by σ, and the polarization vector σ' (π') of the scattered beam is perpendicular (parallel) to the scattering plane. The polarization of the scattered X-ray is analyzed by rotating the analyzer crystal by an angle ϕ_A. The analyzer crystal is selected such that the scattering angle $2\theta_A$ is close to 90°. The σ'-polarized beam is detected by the analyzer with $\phi_A = 0°$, and the structure factor is expressed by $F_{\sigma\sigma'}$ with $\hat{\varepsilon}_i = \sigma$ and $\hat{\varepsilon}_s = \sigma'$. The π'-polarized beam is detected at $\phi_A = 90°$, and the structure factor is expressed by $F_{\sigma\pi'}$.

3 Orbital Ordering in Perovskite Titanate

Perovskite titanate, $YTiO_3$, is a t_{2g} electron system. One electron occupies the triply degenerated t_{2g} orbitals, and it shows typical t_{2g} orbital ordering. Hence, the orbitally ordered state was investigated in depth using the RXS technique, and this became a target next to the e_g orbital-ordering study. This study not only acted as evidence of t_{2g} orbital ordering but also facilitated a discussion of the RXS mechanism. In fact, substances having the e_g electron system such as manganites exhibit considerable JTD owing to a strong electron–lattice coupling; then the scattering mechanism of Coulomb and JT mechanisms became the controversial problem as described above. In contrast, the t_{2g} electron system has a weak electron–lattice coupling. As a result, it is expected that the JT mechanism in the t_{2g} system is less effective in giving rise to RXS when compared with the e_g system. In this section, RXS studies of t_{2g} orbital ordering in $YTiO_3$ [25] and $Y_{1-x}Ca_xTiO_3$ [26, 28, 29] are presented.

3.1 $YTiO_3$

$YTiO_3$ is a ferromagnetic (FM) insulator with $T_C \sim 30\,\mathrm{K}$. The Ti^{3+} ion has one t_{2g} electron, and it shows orbital ordering. Orbital ordering is expected to be the origin of its ferromagnetism and has been studied extensively both theoretically and experimentally. Unrestricted Hartee–Fock calculation [70, 71] and generalized gradient approximation [72] have been employed to predict the wave functions of the orbitally ordered state to be a linear combination of two t_{2g} orbitals at sites $1 - 4$, as shown in Fig. 5. By polarized neutron scattering, spin-density distribution was evaluated, and the wave function of the ordered orbital was determined [73, 74]. The wave function was also estimated by performing an NMR experiment [75]. Both sets of experimental results were consistent with theoretical predictions. However, these techniques can only be used to observe orbital ordering when accompanied by magnetic ordering. Hence, an observation of the orbitally ordered state without magnetic ordering was strongly desired.

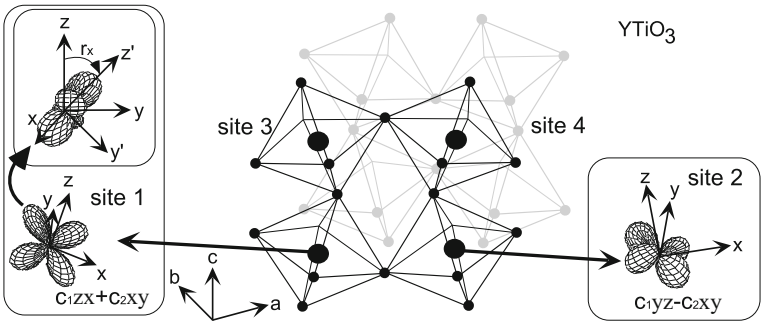

Fig. 5 Orbital ordering in $YTiO_3$. Four Ti sites exist in the unit cell. Ti atoms numbered 1, 2, 3, and 4 are located at $(0, \frac{1}{2}, 0)$, $(\frac{1}{2}, 0, 0)$, $(0, \frac{1}{2}, \frac{1}{2})$, and $(\frac{1}{2}, 0, \frac{1}{2})$, respectively. Wave functions at sites 1, 2, 3, and 4 are $c_1zx + c_2xy$, $c_1yz - c_2xy$, $c_1zx - c_2xy$, and $c_1yz + c_2xy$, respectively. The x, y, and z axes are taken along the directions of Ti–O in the TiO_6 octahedron. The inset of site 1 shows an alternate coordinate system with its axes aligned with the orbital, i.e., the $xy'z'$ coordinates, defined as the xz' plane in which the t_{2g} orbital is elongated. The angle between the z and z' axes following a rotation about the x axis is defined as r_x

To investigate the orbital state of the Ti $3d$ electron above T_C, we performed an RXS study of $YTiO_3$ at room temperature. First, we recorded the X-ray absorption spectrum near the Ti K-edge, as shown in Fig. 6a. We found two large peaks at $E = 4.974$ (main edge) and 4.987 keV, which correspond to the $1s \rightarrow 4p$ dipole transition. The spectrum shows a shoulder feature at $E \sim 4.963$ keV (pre-edge), which corresponds to the $1s \rightarrow 3d$ quadrupole transition energy.

We searched for RXS in the (1 0 0), (0 0 1), and (0 1 1) reflections, which are forbidden reflections on the $Pbnm$ space group. We can expect to observe RXS reflecting orbital ordering at peak positions, as shown in Fig. 5. We measured energy dependence at several azimuthal angles to avoid contamination due to multiple scattering (MS). Strong MS intensity was observed sometimes, and the spectrum was strongly affected, as shown around 4.96 keV in Fig. 7c. The MS intensity can be suppressed by changing the azimuthal angle and incident X-ray energy. In contrast, the real RXS signal changes gradually depending on the azimuthal angle. This is an important point for distinguishing an RXS signal from a spurious signal owing to MS. The data, free of MS, are shown in Fig. 6b–d. The energy spectra depend strongly on the observed reflections. The RXS spectrum at (1 0 0) shows three large resonant peaks at 4.974, 4.986, and 4.999 keV, while that at (0 0 1) shows two large peaks at 4.972 and 4.984 keV. At the pre-edge energy, a small resonant signal was observed for both reflections. Moreover, both RXS spectra have only a $\sigma \rightarrow \pi'$ component. At (0 1 1), both scattering components, $\sigma \rightarrow \sigma'$ and $\sigma \rightarrow \pi'$, were observed simultaneously. Both the components show the same energy dependence, exhibiting two large resonant peaks at 4.975 and 4.986 keV and a weak peak at the pre-edge. In each reflection, several resonant peaks were observed above the main edge energy. In contrast, strong RXS was observed at only one resonant energy (main edge) in the manganite system [5, 6]. The ASF tensor at the main edge is expected to have no

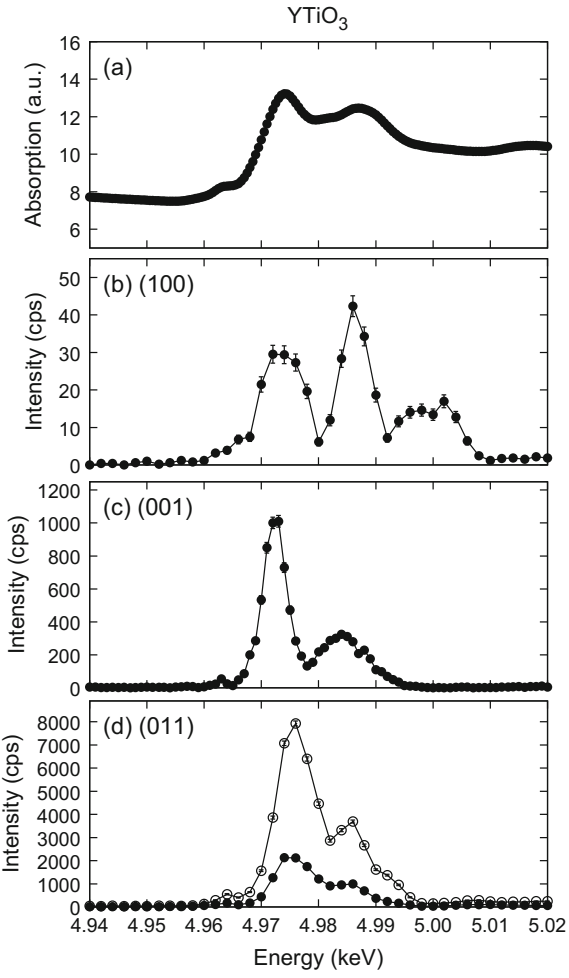

Fig. 6 **a** Absorption spectrum near Ti K-edge energy. **b–d** Energy dependence of RXS intensities at forbidden reflections. Part of data were taken from Ref. [25]. The scattering components $\sigma \rightarrow \sigma'$ and $\sigma \rightarrow \pi$ are shown by *open* and *filled circles*, respectively

radial direction dependence of the scattering vector Q because it is a dipole transition, i.e., the $1s \rightarrow 4p$ transition, as expressed in Sect. 2.2; on the other hand, RXS indicates a marked azimuthal dependence. To clarify the property of RXS, we recorded the energy spectra corresponding to the (0 0 1) and (0 0 3) reflections, which have the same direction of Q and different Q lengths, as shown in Fig. 7a. The energy spectra are quite similar to each other, and RXS intensities are comparable. The quantitative estimation of the scattering intensity is quite difficult near the absorption energy because sample absorption is strong. The spectra at (1 0 0) and (3 0 0) and at (0 1 1) and (0 3 3) are similar to each other, as shown in Fig. 7b, c, respectively. Therefore the ASF tensor at the main edge has no radial direction dependence of Q, which is as expected.

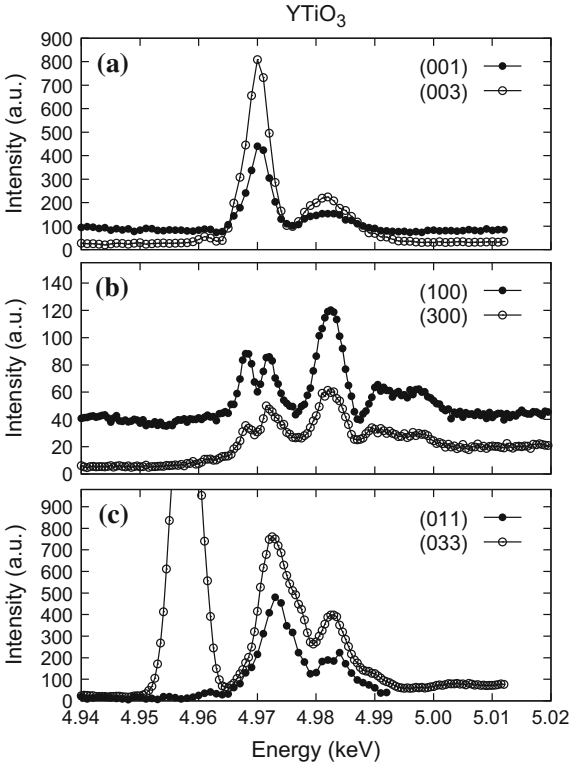

Fig. 7 Energy dependence of RXS intensities for forbidden reflections: **a** (0 0 h), **b** (h 0 0), and **c** (0 h h). To evaluate the radial direction dependence of RXS, the RXS spectra corresponding to the reflections of $h = 1$ are compared with those corresponding to $h = 3$. **c** shows strong MS at around 4.96 keV. Part of data were taken from Ref. [25]

An important feature of RXS is azimuthal angle dependence; the azimuthal angle, Ψ, is a rotation around the scattering vector, as shown in Fig. 4. Azimuthal angle dependence gives direct information about the ASF tensor. Hence, the azimuthal angle dependence of RXS intensity was observed for forbidden reflections at the main edge. At each azimuthal angle, we performed $\theta - 2\theta$ scans. The resulting integrated intensities at (1 0 0), (0 0 1), and (0 1 1) were normalized by those of the fundamental peak of (2 0 0), (0 0 2), and (0 2 2), respectively, to correct any variations due to the sample shape. The structure factors of the fundamental peaks were calculated using crystal parameters [76]. The results were finally normalized by the intensity of (0 2 2) as a standard. The azimuthal angle dependence of the (1 0 0) and (0 0 1) reflections exhibits twofold symmetry, as shown in Fig. 8a, b. For the (0 1 1) reflection, the azimuthal angle dependence of the $\sigma \rightarrow \sigma'$ component shows fourfold symmetry, whereas that of the $\sigma \rightarrow \pi'$ component has a period of 360°, as shown in Fig. 8c, d. Azimuthal angle dependence at the pre-edge was also observed for the (0 0 1) and (0 1 1) reflections, as indicated by open circles in Fig. 8; it was the same as that at the main edge. Moreover, the intensities were normalized by the fundamental peak at the main edge. Hence, correction for the energy dependence of the fundamental peak intensity is needed for a quantitative discussion.

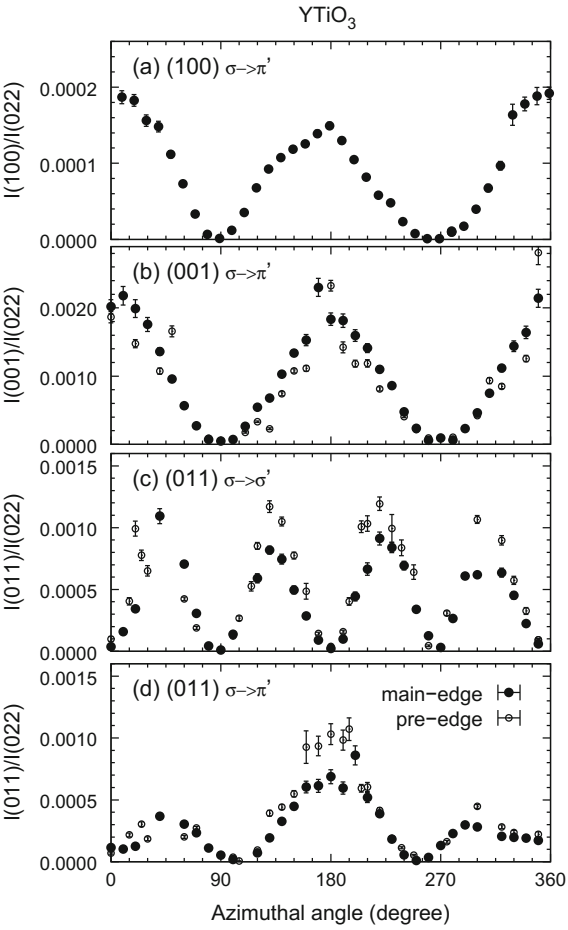

Fig. 8 Azimuthal angle dependence of RXS intensities at (1 0 0) (**a**), (0 0 1) (**b**), and (0 1 1) (**c**, **d**). Data were taken from Ref. [25]. The intensities at the main edge are denoted by *filled circles*, and those at the pre-edge multiplied by 20 are shown by *open circles*. Ψ of the azimuthal angle is defined as follows: **a**, **b** $\Psi = 0°$ at $\sigma \parallel b$; **c**, **d** $\Psi = 0°$ at $\sigma \parallel a$

The origin of RXS is the splitting of the Ti $4p$ energy levels, as indicated in Sect. 2.2. However, the origin of the splitting remains controversial. RXS was calculated on the basis of the Coulomb and JT mechanisms. In the case of the Coulomb mechanism, the Ti $4p$ energy levels are split by on-site Coulomb interaction between the ordered $3d$ orbital and $4p$ orbital of a Ti ion. The wave function, $c_1 zx + c_2 xy$, of the ordered orbital is expected at site 1, as shown in Fig. 5. The wave function is represented by xz' by definition if the principal axes based on xyz coordinates are exchanged for those based on $xy'z'$ coordinates. That is, the t_{2g} orbital is elongated in the xz' plane but not in the y' direction. Because of on-site Coulomb interaction, the $4p_{y'}$ energy level is lowered, and the $4p_x$ and $4p_{z'}$ energy levels are raised. Hence, the tensor at site 1 can be described as follows:

$$\begin{pmatrix} f_a & 0 & 0 \\ 0 & f_a + \Delta f_a & 0 \\ 0 & 0 & f_a \end{pmatrix} \text{ in the } xy'z' \text{coordinates,}$$

where Δf_a is the anisotropic strength and f_a is the isotropic strength of the ASF. The angle between the z and z' axes following a rotation about the x axis is defined as r_x. Thus, the tensor is described with only two parameters: r_x and Δf_a. The tensors at the other three sites are determined in the same manner. These tensors satisfy the space group of the crystal structure $Pbnm$. If the tensors do not satisfy the space group, the azimuthal angle and polarization dependence values calculated from such tensors are completely different from those obtained in the experimental results presented herein. In fact, the azimuthal angle dependence was reported to drastically change in the case of $R\mathrm{VO_3}$ when the space group of the crystal structure was changed, reflecting V $3d$ orbital ordering [36]. Thus, restrictions pertaining to the space group are very strict. Moreover, sites 1–4 have different xyz coordinates owing to the tilting of the $\mathrm{TiO_6}$ octahedron, the so-called $\mathrm{GdFeO_3}$-type structural distortion. In our model calculation, this distortion was considered in terms of the difference of the xyz coordinates among the sites, as explained in Sect. 2.2. On the basis of these tensors, the structure factor can be calculated. The calculated $\sigma \rightarrow \pi'$ components of the intensity at each reflection with $\Psi = 180°$ as a function of r_x are shown in Fig. 9. The intensity ratio among the RXS peaks depends strongly on the value of r_x. The experimentally observed RXS intensities are also plotted on the right ordinate in the figure. In the model calculation, the range of r_x for which the order among the RXS intensities is observed is $30° \sim 70°$. By comparing the measured intensity ratio among the RXS peaks with the calculated value, it is found that $r_x = 45° \pm 10°$, as indicated by an arrow in Fig. 9. The value of $r_x = 45°$ is used to calculate the azimuthal and polarization dependence values of the three reflections. The results of these calculations are shown by lines in Fig. 10. The periodicity and intensity of

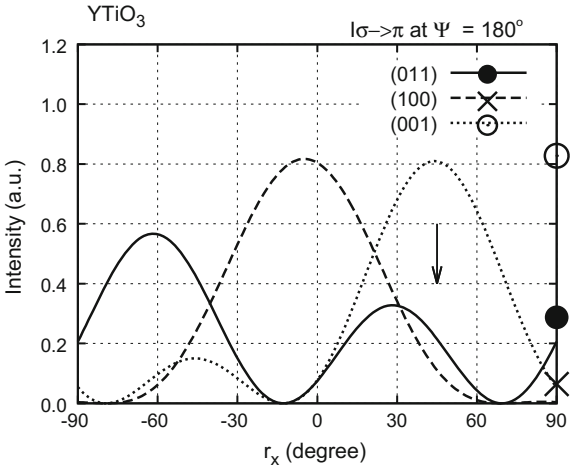

Fig. 9 Rotation angle, r_x, dependence of RXS intensities of the $\sigma \rightarrow \pi'$ component at $\Psi = 180°$. Data were taken from Ref. [25]. The relative intensities observed in the experiments are plotted on the right ordinate

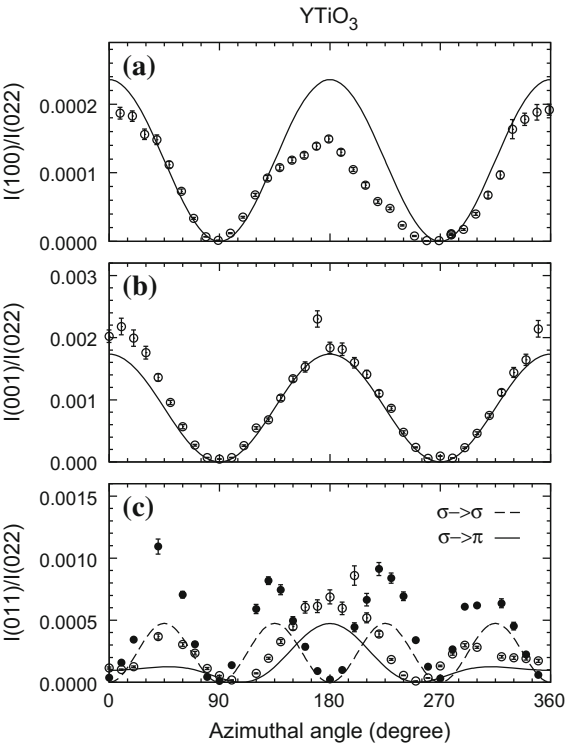

Fig. 10 Azimuthal angle dependence of RXS intensities at the main edge is compared with model calculations using $r_x = 45°$. Data were taken from Ref. [25]. The *solid line* (*open circle*) and *broken line* (*filled circle*) denote the $\sigma \rightarrow \pi'$ and $\sigma \rightarrow \sigma'$ components, respectively

Table 1 Lists of wave function parameters, c_1, determined experimentally and theoretically. The wave function at site 1 is defined as $c_1 zx + c_2 xy$ ($c_1^2 + c_2^2 = 1$)

	c_1
Theory	0.8 [70], 0.71 [72]
Neutron	0.77 [73, 74]
NMR	0.8 [75]
RXS	0.71 [25]

the azimuthal angle dependence were well reproduced by the calculations. Thus, the azimuthal angle and polarization dependence and the intensity ratio among the RXS peaks can be explained by the model calculation that is based on the Coulomb mechanism. It was concluded that the parameters of the wave function of the Ti 3*d* orbital, c_1 and c_2, were $c_1 = 0.71 \pm 0.11$ and $c_1^2 + c_2^2 = 1$, respectively. These values agreed well with the results of previous theoretical and experimental studies within our experimental error bar, as can be inferred from Table 1.

In the case of the JT mechanism, the splitting of the $4p$ energy levels is a result of oxygen movement that distorts the octahedron surrounding the Ti ion in the orbitally ordered state. Then, the tensor is that of the Coulomb mechanism without rotations, i.e., $r_x = 0$ ($c_2 = 0$). It is obvious that $r_x = 0$ required by this simplest version of the JT mechanism cannot explain our results. Hence, it is expected that RXS is mainly caused by the Coulomb mechanism, although a weak RXS signal resulting from the

JT mechanism may exist. However, for quantitative estimation, not only the JTD effect but also the effect of neighboring octahedra should be considered as the origin of RXS, as discussed in the literature [78].

The anisotropic strength of the tensor, Δf_a, determines the intensity ratio between the RXS peak and fundamental peak, while r_x controls the intensity ratio among the RXS peaks. By comparing RXS with the fundamental intensities, Δf_a was determined to be 1.3 ± 0.1. This value was estimated without correction for any extinction effect. For further quantitative estimation, a data-analysis-like structural analysis is required. In addition, the aforementioned Δf_a value was used for the solid curves shown in Fig. 10. It was noted that this Δf_a value was larger than that of $LaMnO_3$ ($\Delta f_a \sim 0.3$), although the JTD was smaller for $YTiO_3$ than that for $LaMnO_3$. Δf_a of $LaMnO_3$ was estimated roughly on the basis of the result in Ref. [6]. This also indicates that the Coulomb mechanism is a plausible model of RXS in $YTiO_3$.

The tensors at the Ti site resulting from the JT and Coulomb mechanisms used in our model calculation are JTD and a simple linear combination of two t_{2g} orbitals, respectively. Thus, we only examined which of these mechanisms is more significant in terms of the origin of RXS. These observations were supportive of the Coulomb mechanism. Ishihara et al. derived a general form for the scattering cross-section of RXS and approached our RXS results as a linear combination of three t_{2g} orbitals [77]. Their wave function parameters better fit our results than those obtained using our simple model calculation. In contrast, Takahashi et al. investigated RXS intensities corresponding to the forbidden reflections using band-structure calculation combined with local density approximation, as shown in Fig. 11 [78]. Accordingly, the calculated RXS intensities arise from not only the JTD but also the tilts of neighboring TiO_6 octahedra. In our JT mechanism model, only the tilt of the octahedra at the site where X-rays are absorbed is considered. The energy spectra obtained theoretically are similar to our experimental results. However, the RXS intensities are comparable in the theoretical calculations of Takahashi et al. Namely the experimental intensity ratio cannot be explained by their theory. There the RXS intensity due to the Coulomb mechanism is expected to be combined with their theory. Moreover, their model leads to a metallic ground state without orbital ordering. Therefore, the experimentally observed RXS intensities at the pre-edge cannot be reproduced by their theory. Finally, this study supports the Coulomb mechanism in the main edge, although other mechanisms also may influence RXS.

We note RXS intensity at the pre-edge. Theoretically, this intensity is expected to directly reflect the $3d$ orbital state, although the precise scattering mechanism is not well understood. In $LaMnO_3$, RXS due to a weak dipole transition arising from the hybridization of Mn $4p$ with neighboring orbitally ordered Mn $3d$s was predicted [66, 68]. In V_2O_3, in contrast, strong RXS was observed at the pre-edge owing to broken local inversion symmetry; on the other hand, no RXS was observed at the main edge [30, 79]. In this study, in $YTiO_3$, the azimuthal angle, polarization, and Q-position dependence at the pre-edge are the same as those at the main edge, and there is inversion symmetry. Therefore, RXS at the pre-edge probably arose from a dipole transition caused by the hybridization of Ti $4p$ with neighboring orbitally ordered Ti $3d$s. Within the experimental error bound, the ratio between

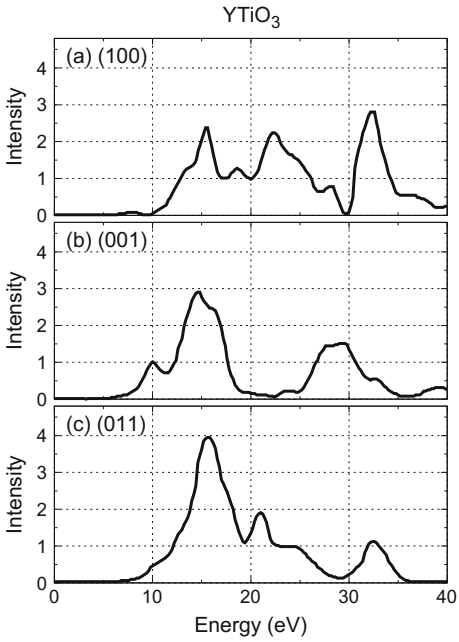

Fig. 11 Theoretical calculations of RXS spectra for (1 0 0), (0 0 1), and (0 1 1) reflections. The origin of the energy corresponds to the photon energy required for exciting an electron from the 1*s* state to the Fermi level. Data were taken from Ref. [78]

intensities at the pre-edge and main edge is almost independent of the reflections. As a result, $r_x \sim 45°$ at the pre-edge was immediately determined. The anisotropic strength of the ASF, $\Delta f_a \sim 0.2$, at the pre-edge was obtained by comparing RXS and the fundamental intensities with correction for the absorption effect. Thus, the ASF tensor at the pre-edge was quantitatively determined.

3.2 $Y_{1-X}Ca_xTiO_3$

In the study of RXS in $YTiO_3$, we discussed the orbital ordering of the 3*d* electron of Ti^{3+}. However, it was expected that the RXS intensity appears to reflect not only the orbital state but also the structural character. Hence, the origin of RXS remains controversial both experimentally and theoretically. The origin of RXS is important for a qualitative discussion of an orbital state. Herein we noted $Y_{1-x}Ca_xTiO_3$, in which orbital ordering is suppressed by Ca substitution [26, 28]. Here, we can discuss the origin of RXS because we expect that RXS signals reflecting the orbital state and structural character show different Ca substitution dependence values. The RXS signal at the Y *K* edge ($1s \rightarrow 5p$ transition energy) was also noted [29]. There we expect that only the RXS intensity due to the octahedral tilt can be observed. By combining the RXS signals at the Ti *K* edge and Y *K* edge, we discuss the origin of RXS. The result elucidates the potential to determine the wave function of the ordered orbital using this RXS technique.

In $Y_{1-x}Ca_xTiO_3$, the number of $3d$ electrons in the Ti ion changes from 1 to 0 on Ca substitution [80–84]. FM ordering disappears at $x_{FP} \sim 0.15$ with increasing x, whereas the insulating state is preserved up to x_{MI}. A marked metal–insulator transition was observed at x_{MI}. Then, the paramagnetic (PM)–metal phase stabilized above x_{MI}. Hence, it was expected that the orbital degree of freedom plays an important role in these phases. The orbitally ordered state was systematically investigated in $Y_{1-x}Ca_xTiO_3$ ($0 \leq x \leq 0.75$) using the RXS technique [26, 28].

RXS intensities at the forbidden reflections, (0 0 1), (1 0 0), and (0 1 1), were searched for near the Ti K-edge energy on the basis of the result obtained using $YTiO_3$. Energy dependence was measured at several azimuthal angles to avoid contamination due to MS. The data, free of MS, are shown in Fig. 12. The (0 0 1),

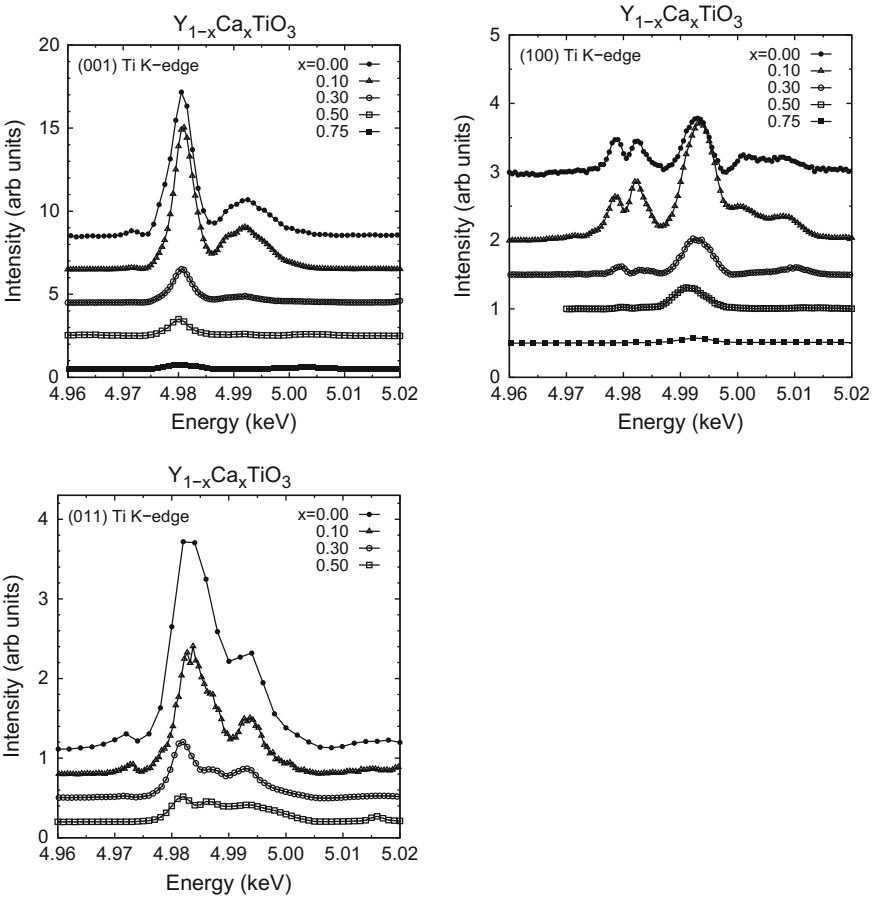

Fig. 12 Energy dependence of RXS intensities of $Y_{1-x}Ca_xTiO_3$ for the forbidden reflections (0 0 1), (1 0 0), and (0 1 1). Data were taken from Refs. [25, 26, 28]. Baselines were shifted for clarity

(1 0 0), and (0 1 1) intensities were normalized by the fundamental reflections, (0 0 2), (2 0 0), and (0 2 2), respectively, to correct any error due to the sample shape. To compare the intensities with those obtained for other Ca concentrations, the intensities were also normalized by the respective structure factors of the fundamental peaks, thus reflecting structural changes with Ca doping [28]. The RXS intensities at (0 0 1) and (0 1 1) decreased monotonically, and the energy spectra indicated no remarkable change with increasing Ca concentration, x. In contrast, the energy spectra at (1 0 0) changed depending on x. The spectra above the main edge changed drastically, while the intensities decreased at the main edge and pre-edge energies. The main edge and pre-edge energies were approximately 4.980 and 4.972 eV, respectively. These energies were different from those defined in Sect. 3.1 because of differences in energy calibration.

Figure 13 shows the Ca concentration dependence of an RXS intensity at the main edge. The RXS intensities decreased gradually with increasing x. The intensity ratio among these peaks was almost the same as a function of x. Next, RXS at the pre-edge, which is expected to be the order parameter of orbital ordering as discussed in Sect. 3.1, is noted. The Ca concentration dependence of the RXS intensities at (0 0 1) and (0 1 1) is shown in Fig. 14b. The intensities decreased rapidly in the concentration range of $0 < x < 0.15$ and could barely be discerned at $x = 0.30$ at the insulator phase. Moreover, the intensity almost disappeared at the metal phase ($x \geq 0.5$). In other words, the orbital ordering of Ti 3*d* was strongly suppressed in the $0 < x < 0.15$ concentration range but barely remained up to x_{MI}. This result is consistent with the results of a structural analysis based on powder X-ray diffraction [28]. Here, the Ca concentration dependence of the RXS intensity at the main edge, as shown in Fig. 14a,

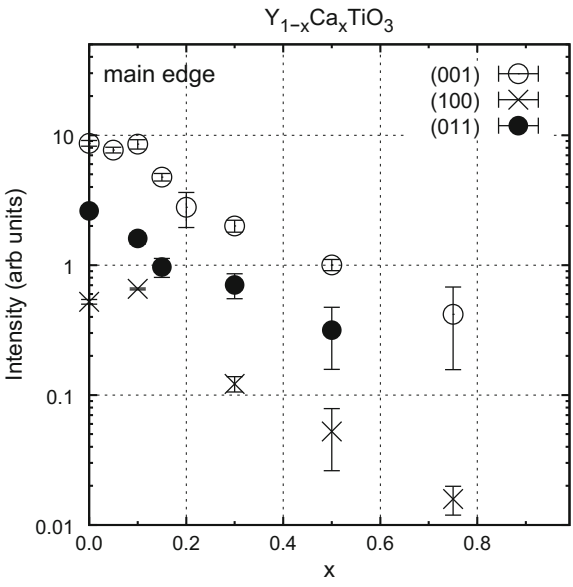

Fig. 13 RXS intensities at main edge energy as a function of x. RXS intensities were normalized by observed and calculated fundamental peak intensities. Data were taken from Ref. [28]

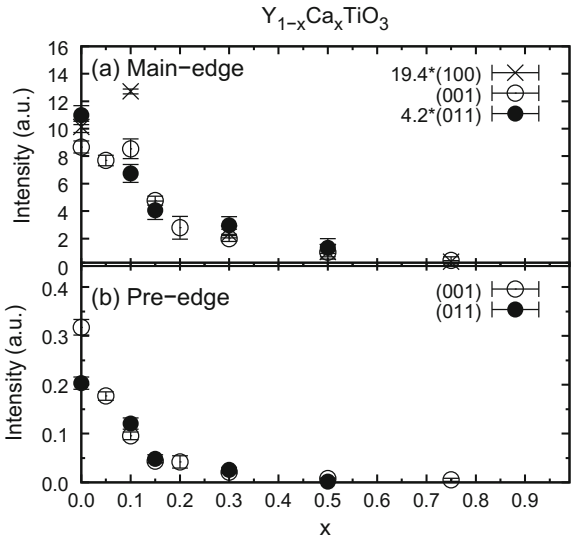

Fig. 14 Ca concentration dependence of RXS intensities **a** at main edge and **b** at pre-edge. Data were taken from Refs. [26, 28]

is considered. The RXS intensity declined with increasing x, and the rate of decrease slowed at $x \sim 0.2$. The dependence is similar to that at the pre-edge. Hence, it can be expected that the RXS at the main edge mainly reflects orbital ordering. However, this RXS intensity remains even at the metal phase ($x > x_{MI}$). The intensity is about 1/10th that of $YTiO_3$ ($x = 0$), and it may reflect the local structure around the Ti ion. As a result, we believe that the Coulomb mechanism is in effect on the main edge because RXS reflects mainly the order parameter of orbital ordering. Moreover, it is important that the other mechanisms have a small effect on RXS.

Precise RXS measurement can be used to quantitatively determine the ASF tensors, r_x and Δf_a. This is purely an experimental result and independent of the scattering mechanism. The intensity ratio among the RXS peaks changed drastically as a function of r_x (Fig. 9). In the case of $Y_{1-x}Ca_xTiO_3$, the intensity ratio was nearly independent of Ca concentration, as shown in Fig. 13. That is, r_x is about 45°, the same value as that reported in the case of $x = 0$. Then, Δf_a was estimated in the case of $YTiO_3$ because the intensity ratio between the RXS peak and fundamental peak reflects the anisotropic strength of the ASF, Δf_a. The Ca concentration dependence of Δf_a was estimated, as shown in Fig. 15. The anisotropic strength of the ASF decreased gradually with increasing x, and it remained in the metallic region ($x > x_{MI}$). At the metal phase, the orbital disordered state was expected. At that state, RXS cannot be explained by the Coulomb and JT mechanisms. The tilt of neighboring octahedra was proposed as the origin of an RXS signal at the metal phase [26, 28]. The Ca concentration dependence of RXS intensity, reflected in the tilt of neighboring octahedra, was expected to be estimated as a function of octahedral tilting.

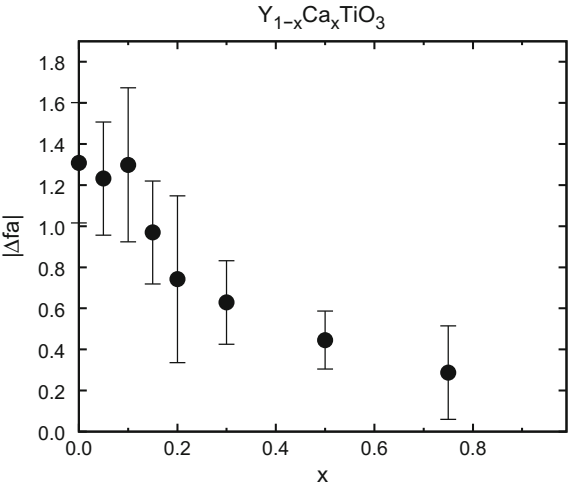

Fig. 15 Anisotropic strength of ASF, Δf_a, as a function of Ca concentration dependence. Data were taken from Ref. [28]

To evaluate RXS, which is reflected in the tilting of the TiO_6 octahedra in a crystal, experimentally, the RXS signal at the Y K edge was noted [29]. In this case, the $1s \rightarrow 5p$ transition was used. Hence, the local environment around the Y ion was detected using the RXS at Y K edge. It was reported that RXS at the La L edge is mainly caused by the tilting of the MnO_6 octahedra in $LaMnO_3$ [16, 85], which has the same crystal structure with the space group, $Pbnm$, as this perovskite titanate system [28, 86]. Therefore, it can be expected that only the RXS intensity due to octahedral tilting can be observed at the Y K edge, whereas RXS at the main edge of Ti K edge reflects both orbital ordering and octahedral tilting.

We searched for the RXS signal at several forbidden reflection positions near the Y K-edge energy to detect RXS reflecting the octahedral tilting. The absorption spectrum of $YTiO_3$ was obtained at the Y K edge, as shown in Fig. 16a. The energy dependence showed clear absorption at the K edge energy. The spectrum was detected to resonate near the Y K edge only at (5 0 0), as shown in Fig. 16b. The intensity had a $\sigma \rightarrow \pi'$ component and not a $\sigma \rightarrow \sigma'$ one. The azimuthal angle dependence of the intensity was measured at $E = 17.033$ keV. The integrated intensities at (5 0 0) were normalized by that of the fundamental peak of (6 0 0). The azimuthal angle dependence exhibited twofold symmetry ($\propto \cos^2 \Psi$), as shown in Fig. 17, and was consistent with the space group.

The energy spectra of RXS were obtained at (5 0 0) as a function of Ca concentration, x, as shown in Fig. 18. The spectra did not change markedly with increasing x. Then, the Ca dependence of the RXS intensity at the azimuthal angle $\Psi = 0°$ was estimated, as shown in Fig. 19a. To avoid error due to MS and sample shape, the intensities at $\Psi = 0°$ were estimated according to the fitting function, $A \cos^2 \Psi$. The fitted result at $x = 0$ is shown in Fig. 17. The obtained intensities normalized by the respective structure factors of the fundamental peak (6 0 0), reflecting the structural change with Ca doping and the number of Y ions. The obtained RXS intensities are

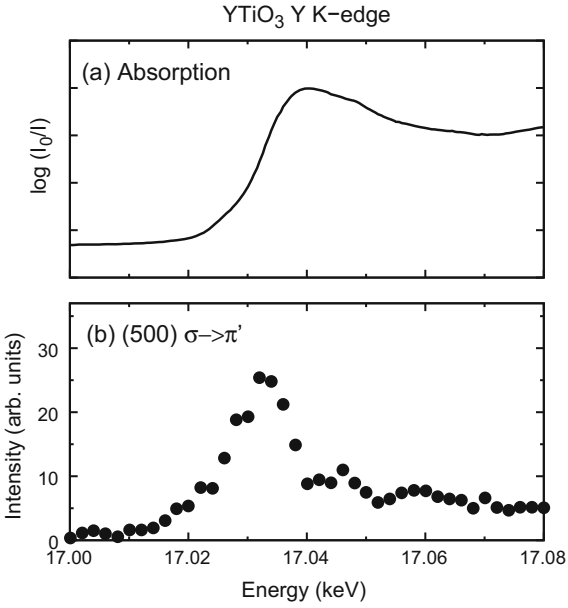

Fig. 16 **a** Absorption spectrum of the $YTiO_3$ powder sample. **b** Energy dependence of RXS intensity at (5 0 0) reflection with $\sigma \rightarrow \pi'$ polarization. Data were taken from Ref. [29]

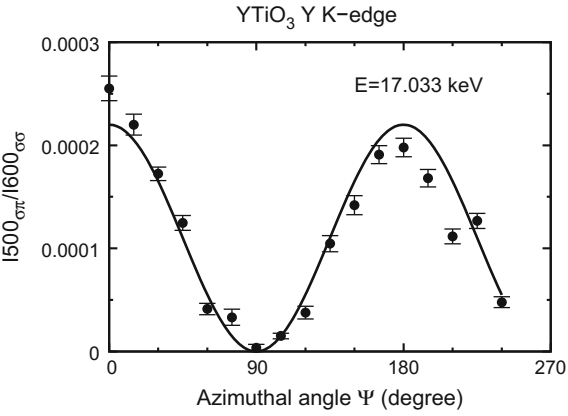

Fig. 17 Azimuthal angle dependence of the scattering intensity with $\sigma \rightarrow \pi'$ polarization at (5 0 0) in $YTiO_3$. Data were taken from Ref. [29]. The azimuthal angle Ψ is defined as $\Psi = 0°$ when the polarization vector σ is parallel to the b axis. The plotted function, $A \cos^2 \Psi$, is represented by the *solid line*

shown in Fig. 19a. The RXS intensities were almost constant in the entire Ca concentration region, whereas the RXS intensities at the Ti K edge decreased markedly with increasing x, as shown in Fig. 19b, c. Figure 19d shows the Ca dependence of the deviation from 180° of the Ti–O–Ti bond angle (Δ_{tilt}). Δ_{tilt} shows no remarkable change and decreases slightly with increasing x. Hence, the Ca dependence of the RXS intensity at Y K edge is similar to that of Δ_{tilt}. Finally, it was expected that the origin of RXS is related to the deviation of the Ti–O–Ti bond angle from 180°, as in the case of RXS at the La L edge in $LaMnO_3$. In the low Ca concentration region ($0 < x < 0.2$), the RXS intensity increased with increasing x, whereas Δ_{tilt}

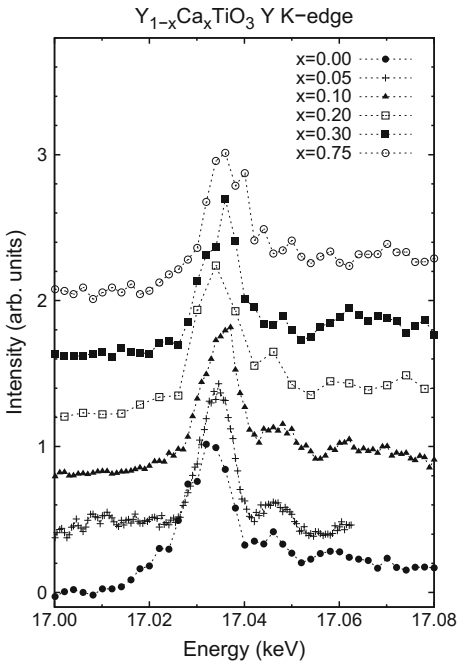

Fig. 18 Energy dependence of RXS intensities as a function of Ca concentration, x. Data were taken from Ref. [29]. The *dotted lines* are visual guides

decreased monotonically. This cannot simply be explained by the RXS associated with the deviation of the Ti–O–Ti bond angle from 180°. It may indicate a difference in the local environment around only the Y ion, while parameters obtained by the structural analysis are the averages of those at the Y and Ca sites. A theoretical study is needed for a detailed discussion of the scattering mechanism.

Here, we focus on the Ca concentration dependence of the RXS intensity at the main edge of the Ti K edge. The RXS intensity at the insulator phase ($0 \leq x < 0.4$) is expected to reflect both orbital ordering and tilts of the octahedra (Δ_{tilt}). The latter origin of RXS is the same as that of RXS at the Y K edge. Therefore, the Ca concentration dependence of the RXS intensity at the main edge of the Ti K edge originating from the Δ_{tilt} ($ITi_{tilt}(x)$) should be similar to that of the RXS intensity at the Y K edge ($IY(x)$, Fig. 19a): the $ITi_{tilt}(x)$ is expected to be almost constant as a function of Ca concentration. Here, the origin of RXS at the main edge of the Ti K edge is discussed considering the following steps: (1) the Ca concentration dependence of $ITi_{tilt}(x)$, (2) Ca concentration dependence of RXS reflecting the orbitally ordered state ($ITi_{OO}(x)$), and (3) evaluation of RXS at the main edge of the Ti K edge using the obtained $ITi_{OO}(x)$ and $ITi_{tilt}(x)$. As the first step, the Ca concentration dependence of $ITi_{tilt}(x)$ was evaluated. The $ITi_{tilt}(x)$ reflects the local crystal structure around the Ti ion, which is under the averaged effect of the Y and Ca ions. In contrast, the RXS intensity at the Y K edge reflects the local structure around only the Y ions. Therefore, the Ca concentration dependence of $ITi_{tilt}(x)$ should be estimated not based on $IY(x)$ but based on the structural

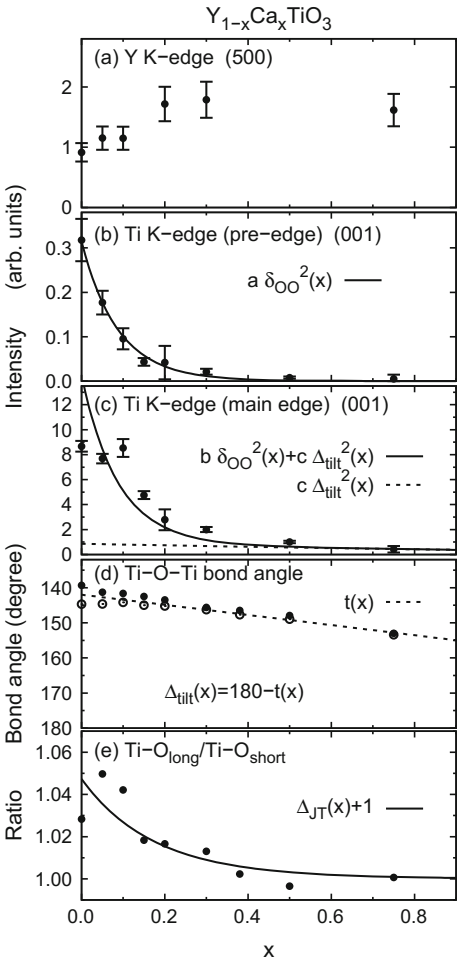

Fig. 19 Ca concentration dependence of the RXS intensity at **a** Y K edge ($E \sim 17.033$ keV), **b** pre-edge, and **c** main edge of the Ti K edge. **d** Ti–O–Ti bond angles in ab plane (*open circles*) and along c axis (*filled circles*) as functions of Ca concentration. **e** Ratio between Ti-O_{long} and Ti-O_{short} in TiO_6 octahedron. These structural parameters were determined via the structural analysis. Data were taken from Refs. [26, 28, 29]

parameter Δ_{tilt}. The Ca concentration dependence values of the average Ti–O–Ti bond angles in the ab plane and along the c axis were fitted by a linear function $t(x)$, as shown in Fig. 19d. To estimate $ITi_{tilt}(x)$, we assumed that the RXS intensity due to the octahedral tilt, $ITi_{tilt}(x)$, is proportional to $\Delta^2_{tilt}(x) = (180 - t(x))^2$; the RXS intensity reflecting the JTD in $LaMnO_3$ was theoretically calculated to be proportional to the square of the distortion [68]. The obtained function, $ITi_{tilt}(x)$, is shown in Fig. 19c by a dotted line, which indicates no marked change over the entire Ca concentration region. Second, we examined $ITi_{OO}(x)$ reflecting the $3d$ orbital state; $ITi_{OO}(x)$ was expected to be proportional to the square of the order parameter of orbital ordering ($\delta_{OO}(x)$) [6]. In orbitally ordered systems, because of the JT effect, the order parameter $\delta_{OO}(x)$ is of the same size as the JTD ($\Delta_{JT}(x)$), i.e., $ITi_{OO}(x) \propto \delta^2_{OO}(x) \propto \Delta^2_{JT}(x)$. In this case, JT distortion was estimated from

the ratio of the longest Ti–O bond length (Ti-O_{long}) and the averaged short Ti–O bond length (Ti-O_{short}) of the TiO_6 octahedron. The Ca concentration dependence was fitted by the function $\Delta_{JT}(x) + 1$ ($\equiv \frac{(\mathrm{Ti-O}_{long})-(\mathrm{Ti-O}_{short})}{(\mathrm{Ti-O}_{short})} + 1 = \frac{(\mathrm{Ti-O}_{long})}{(\mathrm{Ti-O}_{short})}$), as shown by a solid line in Fig. 19e. Thus, the Ca concentration dependence of the order parameter $\delta_{OO}(x)$ was obtained from the figure. The obtained $\delta^2_{OO}(x)$ agreed well with RXS dependence at the pre-edge of the Ti *K* edge, thus reflecting the anisotropy of the 3*d* orbital state directly, as shown by a solid line in Fig. 19b. Consequently, the Ca dependence values of RXS intensities reflecting the octahedral tilt and orbital ordering can be expressed by $\Delta^2_{tilt}(x)$ and $\delta^2_{OO}(x)$, respectively.

Finally, the Ca concentration dependence of the RXS intensity at the main edge of the Ti *K* edge was fitted by $b\delta^2_{OO}(x) + c\Delta^2_{tilt}(x)$, as shown in Fig. 19c by the solid line. The experimental data can be explained sufficiently by the fitted curve. The fitting parameters b and c reflect the extents of energy-level splitting due to orbital ordering and octahedral tilt, respectively. Both parameters have positive values. Therefore, the Ti $4p$ orbital reflecting the on-site Coulomb interaction between the $3d - 4p$ orbitals of the Ti ion and that originating from the tilts of neighboring TiO_6 octahedra may have the same energy-level scheme. At $YTiO_3$ ($x = 0.0$), $ITi_{tilt}(x) = c\Delta^2_{tilt}(x)$ shown by the dotted line in the figure is much smaller than $ITi_{OO}(x) = b\Delta^2_{JT}(x)$. Thus, RXS reflecting orbital ordering was mainly observed at $x = 0.0$, and the wave function of the ordered orbital was determined successfully from the RXS intensity at the main edge of the Ti *K* edge in $YTiO_3$. Using the obtained $ITi_{OO}(x)$, we can discuss the wave function of ordered orbitals over the entire Ca concentration region. However, there remain open questions for our assumptions: whether the Ca concentration dependence of $ITi_{tilt}(x)$ is the same as that of $IY(x)$, whether $ITi_{tilt}(x)$ is proportional to $\Delta^2_{tilt}(x)$, and whether the Ca concentration dependence of $ITi_{OO}(x)$ is the same as that of the RXS intensity at the pre-edge of the Ti *K* edge. To establish the scattering mechanism of RXS, a theoretical study of this mechanism is needed.

Consequently, the origin of RXS at the main edge of the Ti K edge is understood experimentally. It is well explained by considering two origins of RXS, i.e., the orbitally ordered state and structural characteristic. Strong RXS reflecting orbital ordering exists in the case of $YTiO_3$, and the wave function of the ordered 3*d* orbital can be estimated. Therefore, RXS studies of titanate elucidate that the RXS technique is useful for estimating the orbital state, although the origin of RXS needs to be understood.

4 Applications of RXS Measurements

As established above, RXS can be used for determining orbital and charge ordering. As the next step, the RXS technique has been applied to experiments at extreme conditions. Moreover, researchers have attempted to determine new types of electronic ordering states using this technique. Therefore, in this section, we describe

experiments on thin-film systems and high-pressure experiments using a diamond anvil cell as challenging tasks. Observation of the spin-state ordering is provided as a new direction for RXS studies.

4.1 Charge and Orbitally Ordered States in Thin-Film Systems

Pulsed laser deposition has rapidly developed as a technique for fabricating artificial lattices. It can now be used to atomically control the artificial lattice of a perovskite system. In the perovskite structure family, various physical properties, high–temperature superconductivity, multiferroics and colossal magnetoresistance (CMR), have been reported. Hence, many groups have attempted to fabricate superlattices combining different physical properties to create new physical properties and new functions. Strong coupling among charges, spins, and orbitals of $3d$ electrons and lattice degrees of freedom played important roles in those studies. Hence, the study of charge and orbitally ordered states in thin-film systems gained importance, and the RXS technique was applied to various film systems [20–24, 51].

4.1.1 Mn Valence States in $[(LaMnO_3)_m(SrMnO_3)_m]_n$ Thin Film

Perovskite manganites show various interesting phenomena such as CMR because of the close interplay among charges, orbitals, spins, and lattice degrees of freedom. The $[(LaMnO_3)_m(SrMnO_3)_m]_n$ superlattice was fabricated as a stage for artificially controlling the valence of Mn [87]. The films were composed of the same number of $LaMnO_3$ and $SrMnO_3$ layers; thus, the average Mn valence was maintained at 3.5+. The Mn valence values in the $LaMnO_3$ and $SrMnO_3$ layers were 3+ and 4+, respectively. The valence distribution was expected to be determined by the stacking sequence of $LaMnO_3/SrMnO_3$ layers. Recently, a new CMR effect that has never been realized in the (La, Sr)MnO_3 alloy was discovered in this superlattice system [88]. To microscopically understand the physical properties of the $[(LaMnO_3)_m(SrMnO_3)_m]_n$ superlattice, an evaluation of the Mn valence state in the superlattice is very important. Therefore, we attempted to evaluate the valence distribution of Mn ions using the RXS technique on the basis of $I(E, \mathbf{Q})$ near E_a of the Mn ions [24].

For estimating the Mn valence distribution, the ASFs of Mn^{3+} and Mn^{4+} are required, as discussed in Sect. 2. However, it is difficult to determine the ASFs of Mn^{3+} and Mn^{4+} of thin films because fluorescence signals from thin films are quite weak. First, we measured $\mu(E)$ of the bulk $LaMnO_3$ and $SrMnO_3$ samples to estimate the chemical shift between Mn^{3+} and Mn^{4+}. The observed $\mu(E)$ was transformed into the imaginary part of the ASF $f''(E)$ using Eq. (4). The obtained $f''(E)$ spectra are shown in Fig. 20a. E_a of $SrMnO_3$ is approximately 3 eV higher than that of $LaMnO_3$; this represents a chemical shift. These spectra have different energy

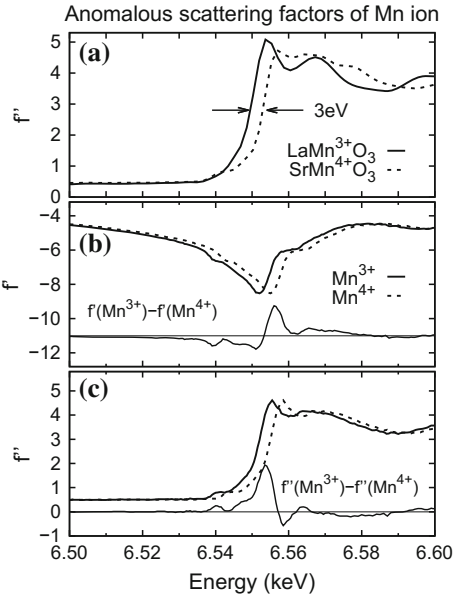

Fig. 20 **a** Anomalous scattering factor $f''(E)$ of $LaMnO_3$ and $SrMnO_3$ bulk. The difference in the absorption-edge energy (E_a) is indicated by *arrows*. **b** $f'(Mn^{3+})$, $f'(Mn^{4+})$, and $f'(Mn^{3+}) - f'(Mn^{4+})$. **c** $f''(Mn^{3+})$, $f''(Mn^{4+})$, and $f''(Mn^{3+}) - f''(Mn^{4+})$. Data were taken from Ref. [24]

profiles above E_a, which reflects the difference in the crystal structure. The ASFs $f'(Mn^{3.5+})$ and $f''(Mn^{3.5+})$ of $La_{0.5}Sr_{0.5}MnO_3$ grown on a $SrTiO_3$ (0 0 1) substrate were obtained from the fluorescence spectra in Ref. [21]. On the basis of the chemical shift of 3 eV, f'' of Mn^{3+} (Mn^{4+}) was obtained from the energy shift of -1.5 eV ($+1.5$ eV) using $f''(Mn^{3.5+})$. $f'(Mn^{3+})$ and $f'(Mn^{4+})$ were calculated according to the Kramers–Krönig transformation of $f''(Mn^{3+})$ and $f''(Mn^{4+})$, respectively [57–59]. The obtained ASFs of Mn^{3+} and Mn^{4+} are shown in Fig. 20b, c, respectively. The differences between the ASFs of Mn^{3+} and Mn^{4+}, i.e., $\Delta f' = f'(Mn^{3+}) - f'(Mn^{4+})$ and $\Delta f'' = f''(Mn^{3+}) - f''(Mn^{4+})$, are strongly enhanced near the Mn K-edge energy, as shown in the figures. Hence, it is expected that a strong signal reflecting the Mn valence distribution will be observed near the energy at superlattice peaks, where the structure factor includes the difference terms $\Delta f'$ and $\Delta f''$.

The crystal structures of the superlattices were evaluated from the Q_z dependence of the scattering intensity, $I(Q_z)$. $I(Q_z)$ around the (0 0 1) reflection of $[(LaMnO_3)_8(SrMnO_3)_8]_6$ is shown in Fig. 21. The superlattice reflections are denoted as $q = \pm 1, \pm 2$, and ± 3 from fundamental reflections, and the peak positions are consistent with $m \sim 8$. The peaks due to the Laue function reflecting $n = 6$ were observed clearly between the superlattice peaks. The peak position at (0 0 1) reflects the lattice constants of the average perovskite structure. The sharp peak at Q_z=1.61 Å^{-1} is the (0 0 1) reflection of the $SrTiO_3$ substrate. $I(Q_z)$ was calculated on the basis of the crystal structure model reported in Ref. [24]. In this case, the superlattice peak positions cannot be explained by periodicities $m = 8$. Hence, the noninteger periodicity $m = 7.6$ was considered. By introducing a noninteger value of m, a La/Sr mixed layer is generated, and the mixing ratio at the interface depends

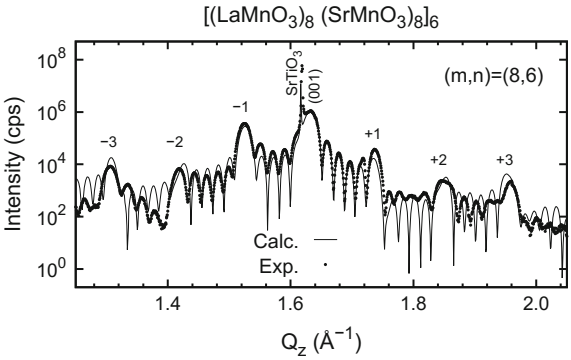

Fig. 21 Diffraction pattern around (0 0 1) of $[(LaMnO_3)_8(SrMnO_3)_8]_6$. Data were taken from Ref. [24]. The model calculation is denoted by the *solid line*

on the parameter m. The out-of-plane lattice constants c_{La} and c_{Sr} were considered in the $LaMnO_3$ and $SrMnO_3$ layers, respectively. Moreover, the relaxation of the lattice constant near the interface between the $LaMnO_3$ and $SrMnO_3$ layers was considered, i.e., the out-of-plane lattice constants expand or contract near the interface to relax lattice distortion. Finally, the parameters used to calculate the scattering intensity of the superlattices are the periodicities m and n; lattice constants in the La/Sr layer c_{La} and c_{Sr}; and lattice relaxation parameter α. The intensity ratios and peak positions are well explained by the model calculation, as indicated by the solid line in Fig. 21. Hence, the crystal structure of the superlattices, which provides sufficient accuracy to estimate the valence state of Mn, was determined.

Then, the energy dependence of the scattering intensity, $I(E, \mathbf{Q})$, was measured at the reflection positions to estimate the valence distribution of Mn ions. $I(E, \mathbf{Q})$ was observed at the fundamental and superlattice reflections shown in Fig. 22. All energy profiles showed strong energy dependence near the Mn K edge. This means that the structure factor includes the ASF of Mn ions. To evaluate energy dependence, four models of Mn valence distribution were considered, as discussed in Ref. [24]. (1) *rect* model: Mn valence in $LaMnO_3$ ($SrMnO_3$) is 3+ (4+), and the valence at the interface has an intermediate value. In the structural model, the periodicity m has a noninteger value, and a La/Sr mixed layer exists. Mn valence at the border of the mixed layer is determined by the La/Sr ratio. Mn valence distribution transforms into an almost rectangular wave. (2) α model: Mn valence is determined by the volume of the perovskite unit cell, the stacking sequence of which is determined by the lattice parameter α. The intermediate valence state occurs in six layers near the interface. (3) *sin* model: Mn valence distribution is a sinusoidal wave from 3+ to 4+, defined as a function of the number of stacking layers. (4) *no* model: All Mn valence values are 3.5+, and there is no charge modulation. On the basis of these valence distribution models, the energy dependence values $I(E, \mathbf{Q})$ were calculated and are shown by the lines in Fig. 22. Valence modulations of the *alpha* and *sin* models are similar to each other in the case of $[(LaMnO_3)_8(SrMnO_3)_8]_6$. Hence, calculation using the *sin* model is not shown here. The structure factor at the fundamental peak (0 0 1) shown in Fig. 22a reflects the average perovskite structure. Hence, the $\Delta f'$

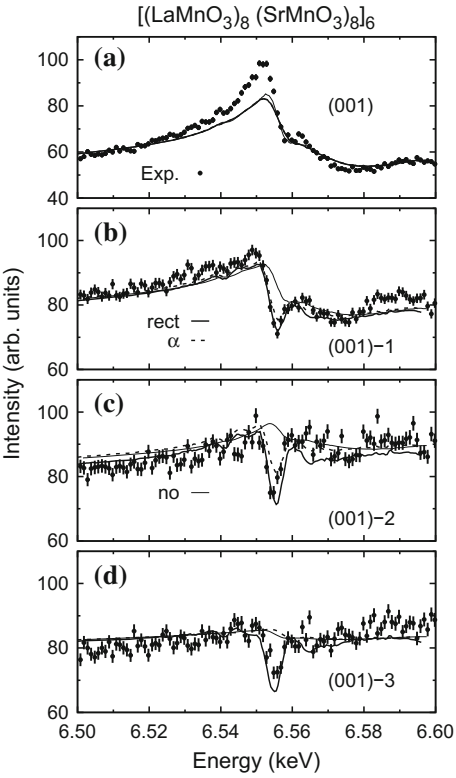

Fig. 22 Energy dependence values of the scattering intensity at **a** (0 0 1), **b** (0 0 1)−1, **c** (0 0 1)−2, and **d** (0 0 1)−3 in $[(LaMnO_3)_8(SrMnO_3)_8]_6$. Data were taken from Ref. [24]. Model calculations are shown by the *thick solid line* (*rect* model), *dashed line* (α model), and *solid line* (*no* model). *no* model: All Mn valence values are 3.5+, and there is no charge modulation. *rect* model: Mn valence in the $LaMnO_3$ ($SrMnO_3$) layer is 3+ (4+), and the valence at the interface has an intermediate value. The Mn valence distribution almost transforms into a rectangular wave. α model: Valence distribution that reflects lattice relaxation near the interface is considered

and $\Delta f''$ terms are canceled in the structure factor, and $I(E, \mathbf{Q})$ is independent of the valence distribution model. In the *no* model, the ASFs of only $Mn^{3.5+}$ are used, whereas in the *rect* and α models, the ASFs of Mn^{3+} and Mn^{4+} are used. Hence, the energy spectrum at the absorption energy of the *no* model is sharper than that of the *rect* model. Next, the energy dependence values of the superlattice peak intensity $I(E, \mathbf{Q})$ were compared with those obtained from model calculations. The resonant peaks near the Mn K edge reflected the existence of the $\Delta f'$ and $\Delta f''$ terms in the structure factor. For all distribution models except the *no* valence distribution model, $I(E, \mathbf{Q})$ at (0 0 1)−1 showed similar energy dependence. With increasing q, the dependence of the α model quickly approached that of the *no* model. In contrast, the *rect* model showed a strong resonant peak near the Mn K-edge energy, even at $q = -3$. Thus, peak height is important for evaluating the valence distribution. Finally, Mn valence distribution in thin-film systems were effectively evaluated using this RXS technique.

4.1.2 Observation of Orbital Superlattice

The observation of orbital states in thin-film systems using the RXS technique has recently become an issue. The structural and physical properties of $La_{1-x}Sr_xMnO_3$ ($x = 0.40$, 0.55) single-layer films and the superlattices of these films have been investigated systematically, and it was proposed that an orbital superlattice (Fig. 23b) can be realized in their films [89]. The in-plane lattices of both $La_{0.45}Sr_{0.55}MnO_3$ and $La_{0.60}Sr_{0.40}MnO_3$ layers grown epitaxially on $SrTiO_3$ (0 0 1) substrates expanded to match that of the substrates as $a = 0.391$ nm. The out-of-plane lattices shortened elastically as $c = 0.379$ and 0.384 nm for the $La_{0.45}Sr_{0.55}MnO_3$ and $La_{0.60}Sr_{0.40}MnO_3$ layers, respectively. The $La_{0.45}Sr_{0.55}MnO_3$ film exhibited antiferromagnetic and metallic ground states, and the $d_{x^2-y^2}$-type orbitals were considered to be occu-

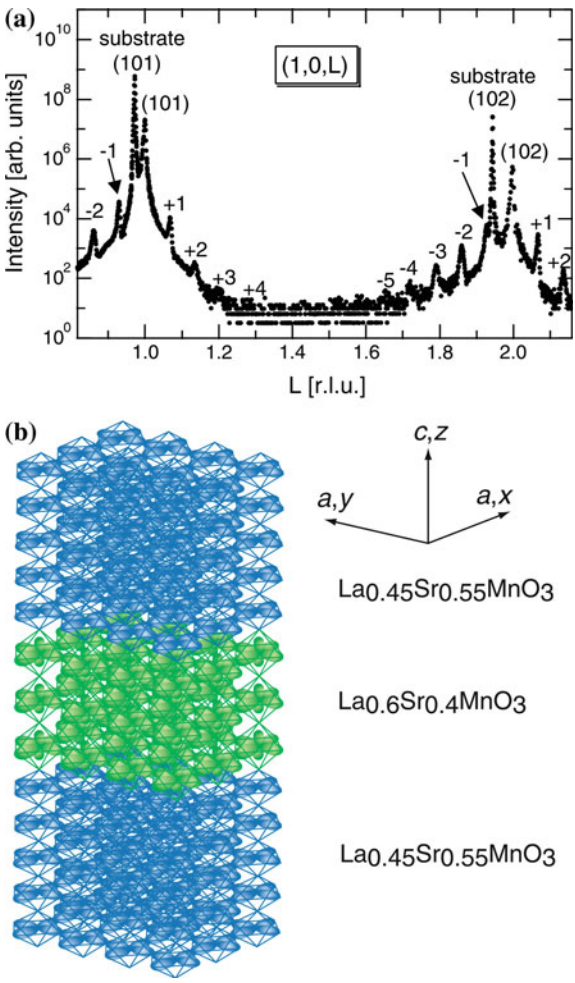

Fig. 23 **a** X-ray diffraction pattern of $[(La_{0.45}Sr_{0.55}MnO_3)_{10}(La_{0.60}Sr_{0.40}MnO_3)_3]_{20}$] superlattices along the (1 0 L) direction in reciprocal space. **b** Schematic of e_g orbital states in $[(La_{0.45}Sr_{0.55}MnO_3)_{10}(La_{0.60}Sr_{0.40}MnO_3)_3]_{20}$] orbital superlattices. $(x^2 - y^2)$-type orbitals in the $x = 0.55$ layers and $(x^2 - y^2)/(3z^2 - r^2)$ disordered orbitals in the $x = 0.40$ layers are shown. Reprinted with permission from Ref. [20] (Copyright 2002 The Physical Society of Japan)

pied through the distortion. By contrast, a disordered orbital state was expected to be realized in the $La_{0.60}Sr_{0.40}MnO_3$ film, which showed metallic conductivity and three-dimensional FM ordering below $T_C = 330-340$ K. These results suggest that these layers preserve their structural and physical properties even in superlattices as in thin films. Therefore, the superlattice is expected to form orbital superlattices, as shown in Fig. 23b, with layered units of different orbital states stacked alternately. To elucidate the orbital superstructure, the interference technique was proposed to observe RXS reflections from ferro-type orbital ordering in the superlattices [20].

The diffraction pattern of $[(La_{0.45}Sr_{0.55}MnO_3)_{10}\,(La_{0.60}Sr_{0.40}MnO_3)_3]_{20}$ along the (1 0 L) direction is shown in Fig. 23a. The satellite peaks between the fundamental peaks (1 0 1) and (1 0 2) indicate successful construction of the superlattices. The satellite peaks are denoted as $\ldots, -1, 0, +1, \ldots$ from fundamental reflections in the stacking direction. To detect the RXS signal reflecting the orbital state, we used X-ray energy near the Mn K-absorption-edge energy E_a. Here, we noted the polarization and azimuthal angle dependence values of the scattering intensity, which indicate that the ASF becomes a tensor near E_a. However, the RXS signal is considerably weaker than that of the Thomson scattering, reflecting the superstructure; in other words, the intensity shown in Fig. 23a mainly reflects the Thomson scattering. The interference technique was used here. The scattering formula in the case of using a polarization analyzer is given as

$$\begin{aligned} I &\propto |F_{\sigma\sigma'}\cos\phi_A - F_{\sigma\pi'}\sin\phi_A|^2 \\ &= |F_{\sigma\sigma'}|^2\cos^2\phi_A - 2Re\{F_{\sigma\sigma'}F^*_{\sigma\pi'}\}\cos\phi_A\sin\phi_A \\ &\quad + |F_{\sigma\pi'}|^2\sin^2\phi_A. \end{aligned} \tag{11}$$

$F_{\sigma\sigma'}$ mainly reflects the Thomson scattering. $F_{\sigma\pi'}$ reflects the tensor of the ASF, namely, the orbital state, and it contains a $\sin\Psi$ term; Ψ is the azimuthal angle, which is defined as $\Psi = 0°$ at $\sigma \perp c$. ϕ_A is the analyzer rotation angle, as shown in Fig. 4. In a weak-$F_{\sigma\pi'}$ case, it is difficult to detect the third term. Hence, the RXS signal can be measured effectively using the second interference term $F_{\sigma\sigma'}F^*_{\sigma\pi'}$. Then, the interference term can be derived by subtracting the intensity at $\phi_A = 97.5°$ from that at $\phi_A = 82.5°$. The energy dependence of the interference term at (1 0 2)+1 indicates a resonating feature near E_a, as shown in Fig. 24a. Reflecting the existence of the $\sin\Psi$ term, the spectrum at $\Psi = \pm 90°$ is inverted and that at $\Psi = 0°$ loses its signal. The azimuthal angle dependence of the interference term is shown in Fig. 24b. The dependence is explained clearly by the $\sin\Psi$ term, denoted by the solid line. These energy, polarization, and azimuthal angle dependence values are consistent with the orbital superlattice structure, as shown in Fig. 23b. The magnitude of the $4p$ energy split ($\Delta E = E_{4p_{xy}} - E_{4p_z}$) is also estimated using the energy spectrum of the interference term. Finally, the values of ΔE in $La_{0.45}Sr_{0.55}MnO_3$ and $La_{0.60}Sr_{0.40}MnO_3$ layers were calculated to be -1.3 and -0.9 eV, respectively. This is clear evidence of the existence of an orbital superlattice in which layers with different orbital states are stacked alternately on the atomic scale. This study became

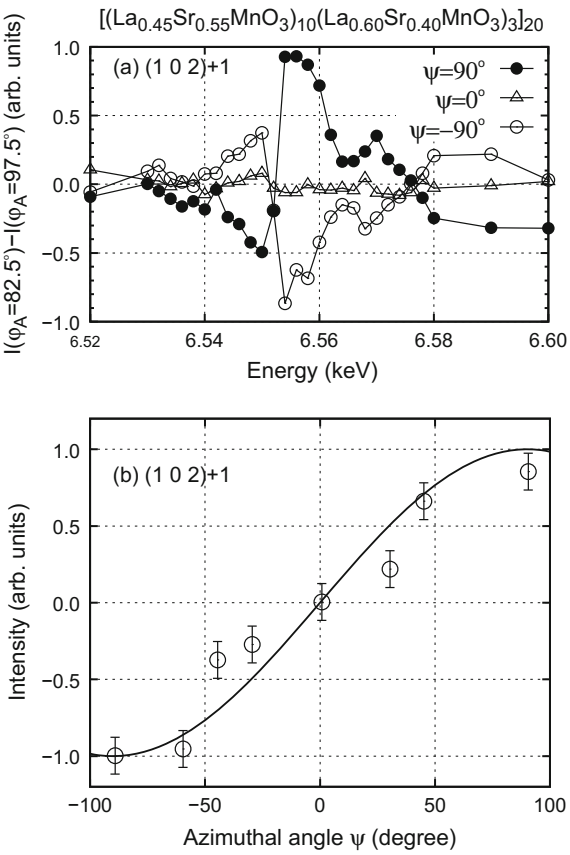

Fig. 24 **a** Energy dependence of interference term at (1 0 2)+1 reflection with azimuthal angles $\Psi = 90°$, 0° and 90°. **b** Azimuthal angle dependence of intensity of interference term at (1 0 2)+1 reflection. Data were taken from Ref. [20]

not only the first experiment to determine orbital ordering using the interference term but also direct observation of a $4p$ energy level. It led to a study of RXS scattering mechanism based on the proposed technique [21, 22].

4.2 RXS Study Under High Pressure

Under high pressure, various intriguing physical properties were discovered in SCES. In this case, the strong correlation among the orbital, charge, and spin degrees of freedom plays an important role. Hence, studying orbital and charge states is very important. In the RXS experiment, however, X-ray energy cannot be selected freely because it is determined by the absorption energy of the target ion. The K-absorption energy of a $3d$ transition metal is low for a high-pressure experiment because X-rays are absorbed strongly by high-pressure cells. Hence, RXS measurement under

high pressure is generally difficult [34, 90]. Here, the Devil's Staircase-type phase transition in NaV_2O_5 under high pressure is presented.

The exciting phase diagram-Devil's flower-was reproduced perfectly in a temperature-pressure phase diagram of NaV_2O_5 [91]. Application of high pressure leads to changes in lattice modulation along the *c*-axis of NaV_2O_5. A precise X-ray diffraction experiment clarified that a large number of transitions occur successively among higher-order commensurate phases. Moreover, NaV_2O_5 is well described as a quarter-filled two-leg ladder system, and all vanadium ions have an average valence state of $V^{4.5+}$. In other words, the system has a charge degree of freedom. Then, NaV_2O_5 undergoes a novel cooperative phase transition associated with its charge disproportionation ($2V^{4.5+} \rightarrow V^{4+} + V^{5+}$) at $T_C = 34\,\mathrm{K}$ [31]. Therefore, the relationship between vanadium charge ordering and the Devil's flower-type phase diagram is important.

To elucidate charge ordering state under high pressure, an RXS experiment was performed [34]. Since 5.47 keV (energy of the *K*-absorption edge of vanadium) X-rays cannot penetrate diamond anvils, a He-gas-driven diamond anvil cell (DAC) using a Be gasket was developed, as shown in Fig. 25. X-rays with an energy of 5.47 keV enter and exit the sample chamber through the Be gasket. As a result, RXS spectra were measured successfully using the DAC, as shown in Fig. 26. A sharp peak structure was observed at approximately 5.468 keV, which corresponds to the $1s \rightarrow 3d$ transition energy (pre-edge). The peak at approximately 5.475 keV corresponds to the main edge energy. At the pre-edge, the peak intensity decreases considerably, while that at the main edge remains almost constant. Here, the intensity at the main edge is dominated by the order parameter δ of charge ordering ($V^{4.5+\delta} + V^{4.5-\delta} \leftarrow 2V^{4.5+}$). This indicates that full charge disproportionation is achieved even in the

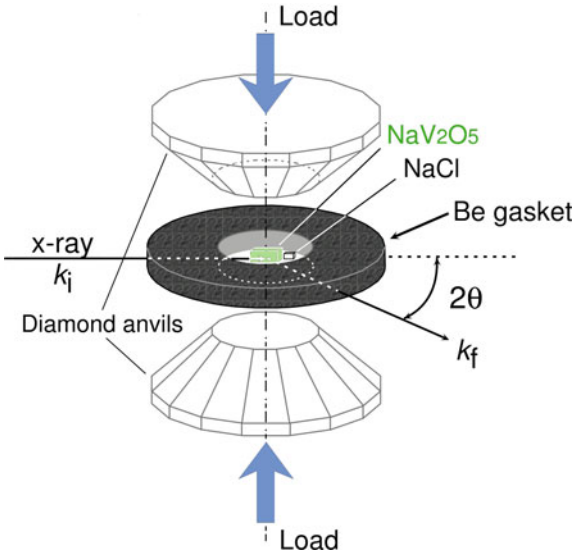

Fig. 25 Layout of RXS-DAC. Four windows were opened on the DAC jacket, each with a 70° equatorial, to allow for the collection of high-angle diffraction of NaV_2O_5 through the Be gasket. Our target reflection (7.5, 0.5, L) was located at $2\theta \sim 100°$ when the incident X-ray energy was 5.47 keV

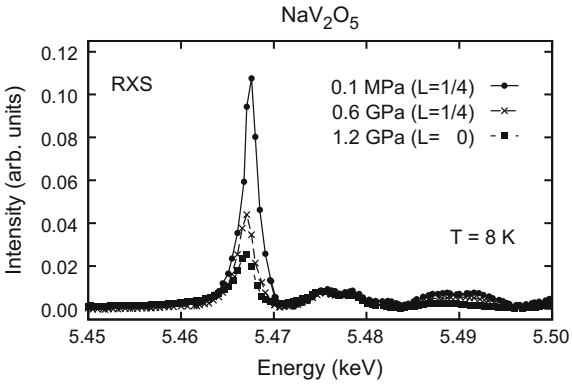

Fig. 26 Energy spectra at $Q = (15/2, 1/2, L)$ observed at 0.1 MPa ($L = 1/4$, $C_{1/4}$ phase), 0.6 GPa ($L = 1/4$, $C_{1/4}$ phase), and 1.2 GPa ($L = 0$, C_0 phase) at 8 K. Data were taken from Ref. [34]

phase under high pressure. In contrast, the intensity at the pre-edge sensitively reflects the breaking size of the local centrosymmetry around the V ion. This indicates that the breaking size of local centrosymmetry decreases with increasing pressure, which is consistent with the obtained crystal structure. This study clarified the possibility of RXS studies under high pressure by using the developed DAC.

4.3 Spin State Study by RXS

The ordered states of charge, spin, and orbital degrees of freedom play important roles in the appearance of many interesting physical properties in SCES. Moreover, spin-state degrees of freedom such as low-spin (LS), high-spin (HS), and intermediate-spin (IS) state emerge additionally depending on the type of ion. In cobalt oxides, a wide variety of physical properties associated with the spin state are expected. In $LaCoO_3$, the ground state of the Co^{3+} ion is a nonmagnetic LS state (t_{2g}^6, $S = 0$). The compound exhibits a gradual transition to a PM phase with increasing temperature [92]. The spin state in the PM phase has been debated, that is, it is controversial whether the moment arises from the IS ($t_{2g}^5 e_g^2$, $S = 1$) [93, 94] or HS ($t_{2g}^4 e_g^2$, $S = 2$) state of the Co^{3+} ion [95–97]. The possibility of the e_g orbital ordering of the IS state was suggested in the PM phase [94]. e_g orbital ordering provides crucial evidence of the existence of an IS state because only the IS state has e_g orbital degrees of freedom. However, there is still no clear evidence for e_g orbital ordering, and the existence of the IS state is a highly controversial issue.

$Sr_3YCo_4O_{10.5}$ is an unusual room-temperature ferrimagnet with $T_C \sim 370$ K, which is the highest T_C among perovskite Co oxides [98–100]. The Curie constant indicates the existence of the IS and/or HS state of the Co^{3+} ion. The crystal structure has been investigated by powder X-ray diffraction, and orbital ordering of the IS state of Co^{3+} has been proposed as the origin of its magnetism [101]. Therefore, this material is a good target for studying the spin states of the Co ion, and an RXS experiment has been performed [48].

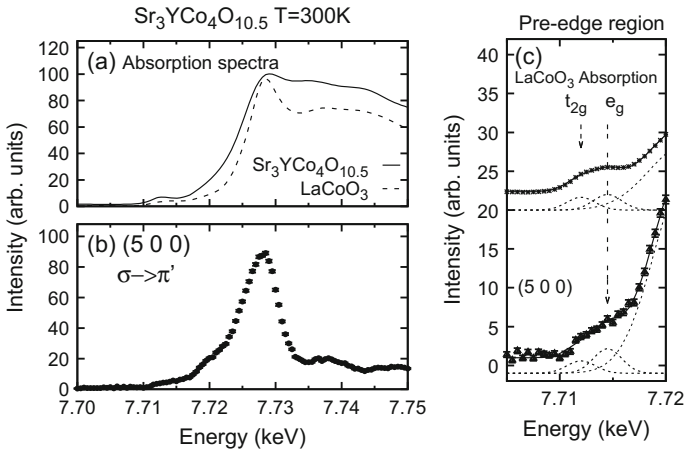

Fig. 27 **a** Absorption spectra of $Sr_3YCo_4O_{10.5}$ (*solid line*) and $LaCoO_3$ (*dashed line*). **b** Energy dependence of scattering intensity at (5 0 0) for $\varepsilon_\sigma \parallel b$. **c** *Bottom* energy dependence of (5 0 0) reflection magnified near pre-edge; *top* absorption spectrum of $LaCoO_3$. Data were taken from Ref. [48]. The *solid lines* show the results fitted with three peaks (*dashed line*). The base lines are shifted for clarity. The *arrows* indicate the $1s \rightarrow t_{2g}$ and e_g transition energies

The absorption spectra of $Sr_3YCo_4O_{10.5}$ are shown in Fig. 27a. The peaks at about 7.713 and 7.728 keV correspond to the pre-edge and main edge energies, respectively. We searched for the RXS signal near the Co K-edge energy to elucidate Co $3d$ orbital ordering. Resonating signals at a series of reflections, $(h\ 0\ 0)$: $h = 4n \pm 1$, were found. The energy spectrum at (5 0 0) is shown in Fig. 27b. The RXS signal has only the $\sigma \rightarrow \pi'$ scattering component. The azimuthal angle dependence exhibits clear twofold symmetry. The intensity peaks at $\sigma \parallel b$ and becomes zero at $\sigma \parallel c$. A significant h dependence of RXS intensity at $(h\ 0\ 0)$ was found as well. On the basis of these results, antiferro-type orbital ordering was proposed, as shown in Fig. 28. Next, the RXS signal at the pre-edge was noted to clarify e_g orbital ordering of the IS state. The absorption spectrum of $LaCoO_3$ has a broad peak (Fig. 27c top) composed of two peaks. The spectrum in the pre-edge region was fitted with two peaks and the tail of the main edge. The high (low)-energy peak corresponds to the $1s \rightarrow e_g$ (t_{2g}) transition. Hence, the t_{2g} and e_g orbital states can be observed separately by tuning the X-ray energy. The energy dependence of the (5 0 0) intensity has a broad peak near the pre-edge energy, and the fitted result clearly indicates the presence of the RXS signal at the $1s \rightarrow e_g$ transition energy. This is direct evidence of not only e_g orbital ordering but also the presence of the IS state because the signal at the $1s \rightarrow e_g$ transition energy reflects the anisotropy of the e_g orbital, and only the IS state has the e_g orbital degrees of freedom. Finally, this RXS study provided us with direct evidence of the existence of the IS state of Co^{3+} and proposed peculiar HS/IS spin-state ordering.

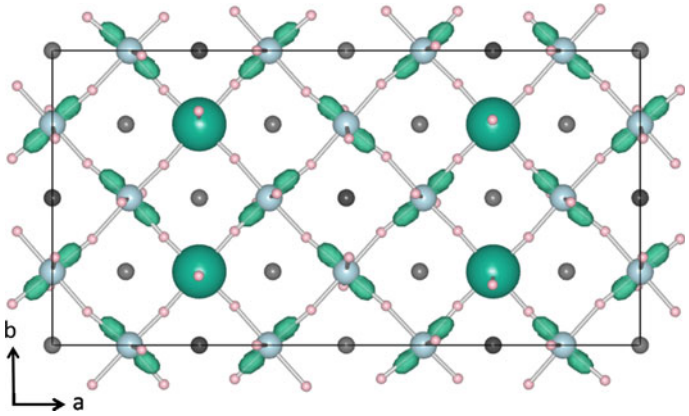

Fig. 28 Orbital and spin ordering structures in CoO_6 layer. The unit cell is indicated by the *solid line*

5 Summary

We reviewed the foundation of the RXS technique and its various applications in 3*d* electron systems. The theoretical framework of the RXS technique was summarized in Sect. 2. In Sect. 3, RXS studies of the perovskite titanate system were presented. It was clarified that the RXS technique can be used to determine orbitally ordered states on the basis of a discussion of the scattering mechanism. In Sect. 4, we presented applications of the RXS technique, namely, charge and orbital ordering in film systems, RXS studies under high pressure, and study of unique spin-state ordering. These indicate the applicability of the technique to resolving typical issues pertaining to the ordering of electronic degrees of freedom. The RXS technique is a powerful technique for investigating charge and orbital ordering in 3*d* transition metal oxides, as described in this chapter. Recently, RXS studies at the $L_{2,3}$ edge (the $2p \rightarrow 3d$ transition energy) have been performed widely. Because the RXS signal at the $L_{2,3}$ edge can directly probe the 3*d* electronic state, a strong magnetic signal of RXS was reported. Furthermore, resonant soft-X-ray scattering was performed globally, as presented in Chap. 5.

References

1. V.E. Dmitrienko, Acta Crystallogr. Sect. A **39**, 29 (1983)
2. D.H. Templeton, L.K. Templeton, Acta Crystallogr. A **41**, 133 (1985)
3. D.H. Templeton, L.K. Templeton, Acta Crystallogr. A **41**, 365 (1985)
4. D.H. Templeton, L.K. Templeton, Acta Crystallogr. A **42**, 478 (1986)
5. Y. Murakami, H. Kawada, H. Kawata, M. Tanaka, T. Arima, Y. Moritomo, Y. Tokura, Phys. Rev. Lett. **80**, 1932 (1998)

6. Y. Murakami, J.P. Hill, D. Gibbs, M. Blume, I. Koyama, M. Tanaka, H. Kawata, T. Arima, Y. Tokura, K. Hirota, Y. Endoh, Phys. Rev. Lett. **81**, 582 (1998)
7. M. Imada, A. Fujimori, Y. Tokura, Rev. Mod. Phys. **70**, 1039 (1998)
8. Y. Tokura, N. Nagaosa, Science **288**, 462 (2000)
9. T.A.W. Beale, G. Beutier, S.R. Bland, A. Bombardi, L. Bouchenoire, O. Bunău, S. Di Matteo, J. Fernández-Rodríguez, J.E. Hamann-Borrero, J. Herrero-Martín, V.L.R. Jacques, R.D. Johnson, A. Juhin, T. Matsumura, C. Mazzoli, A.M. Mulders, H. Nakao, J. Okamoto, S. Partzsch, A.J. Princep, V. Scagnoli, J. Strempfer, C. Vecchini, Y. Wakabayashi, H.C. Walker, D. Wermeille, Y. Yamasaki, Eur. Phys. J. Spec. Top. **208**, 89 (2012)
10. T. Matsumura, H. Nakao, Y. Murakami, J. Phys. Soc. Jpn. **82**, 021007 (2013)
11. Y. Endoh, K. Hirota, S. Ishihara, S. Okamoto, Y. Murakami, A. Nishizawa, T. Fukuda, H. Kimura, H. Nojiri, K. Kaneko, S. Maekawa, Phys. Rev. Lett. **82**, 4328 (1999)
12. K. Nakamura, T. Arima, A. Nakazawa, Y. Wakabayashi, Y. Murakami, Phys. Rev. B **60**, 2425 (1999)
13. M.V. Zimmermann, J.P. Hill, D. Gibbs, M. Blume, D. Casa, B. Keimer, Y. Murakami, Y. Tomioka, Y. Tokura, Phys. Rev. Lett. **83**, 4872 (1999)
14. Y. Wakabayashi, Y. Murakami, Y. Moritomo, I. Koyama, H. Nakao, T. Kiyama, T. Kimura, Y. Tokura, N. Wakabayashi, J. Phys. Soc. Jpn. **70**, 1194 (2001)
15. M.V. Zimmermann, C.S. Nelson, J.P. Hill, D. Gibbs, M. Blume, D. Casa, B. Keimer, Y. Murakami, C.-C. Kao, C. Venkataraman, T. Gog, Y. Tomioka, Y. Tokura, Phys. Rev. B **64**, 195133 (2001)
16. M.V. Zimmermann, C.S. Nelson, Y.-J. Kim, J.P. Hill, D. Gibbs, H. Nakao, Y. Wakabayashi, Y. Murakami, Y. Tokura, Y. Tomioka, T. Arima, C.-C. Kao, D. Casa, C. Venkataraman, T. Gog, Phys. Rev. B **64**, 064411 (2001)
17. J. Voigt, J. Persson, J.W. Kim, G. Bihlmayer, T. Brückel, Phys. Rev. B **76**, 104431 (2007)
18. D. Mannix, D.F. McMorrow, R.A. Ewings, A.T. Boothroyd, D. Prabhakaran, Y. Joly, B. Janousova, C. Mazzoli, L. Paolasini, S.B. Wilkins, Phys. Rev. B **76**, 184420 (2007)
19. R.A. Ewings, A.T. Boothroyd, D.F. McMorrow, D. Mannix, H.C. Walker, B.M.R. Wanklyn, Phys. Rev. B **77**, 104415 (2008)
20. T. Kiyama, Y. Wakabayashi, H. Nakao, H. Ohsumi, Y. Murakami, M. Izumi, M. Kawasaki, Y. Tokura, J. Phys. Soc. Jpn. **72**, 785 (2003)
21. H. Ohsumi, Y. Murakami, T. Kiyama, H. Nakao, M. Kubota, Y. Wakabayashi, Y. Konishi, M. Izumi, M. Kawasaki, Y. Tokura, J. Phys. Soc. Jpn. **72**, 1006 (2003)
22. Y. Wakabayashi, D. Bizen, H. Nakao, Y. Murakami, M. Nakamura, Y. Ogimoto, K. Miyano, H. Sawa, Phys. Rev. Lett. **96**, 017202 (2006)
23. Y. Wakabayashi, D. Bizen, Y. Kubo, H. Nakao, Y. Murakami, M. Nakamura, Y. Ogimoto, K. Miyano, H. Sawa, J. Phys. Soc. Jpn. **77**, 014712 (2008)
24. H. Nakao, J. Nishimura, Y. Murakami, A. Ohtomo, T. Fukumura, M. Kawasaki, T. Koida, Y. Wakabayashi, H. Sawa, J. Phys. Soc. Jpn. **78**, 024602 (2009)
25. H. Nakao, Y. Wakabayashi, T. Kiyama, Y. Murakami, M.V. Zimmermann, J.P. Hill, D. Gibbs, S. Ishihara, Y. Taguchi, Y. Tokura, Phys. Rev. B **66**, 184419 (2002)
26. H. Nakao, M. Tsubota, F. Iga, K. Uchihira, T. Nakano, T. Takabatake, K. Kato, Y. Murakami, J. Phys. Soc. Jpn. **73**, 2620 (2004)
27. M. Kubota, H. Nakao, Y. Murakami, Y. Taguchi, M. Iwama, Y. Tokura, Phys. Rev. B **70**, 245125 (2004)
28. M. Tsubota, F. Iga, K. Uchihira, T. Nakano, S. Kura, T. Takabatake, S. Kodama, H. Nakao, Y. Murakami, J. Phys. Soc. Jpn. **74**, 3259 (2005)
29. H. Nakao, S. Kodama, K. Kiyoto, Y. Murakami, M. Tsubota, F. Iga, K. Uchihira, T. Takabatake, H. Ohsumi, M. Mizumaki, N. Ikeda, J. Phys. Soc. Jpn. **75**, 094706 (2006)
30. L. Paolasini, C. Vettier, F. de Bergevin, F. Yakhou, D. Mannix, A. Stunault, W. Neubeck, M. Altarelli, M. Fabrizio, P.A. Metcalf, J.M. Honig, Phys. Rev. Lett. **82**, 4719 (1999)
31. H. Nakao, K. Ohwada, N. Takesue, Y. Fujii, M. Isobe, Y. Ueda, M.V. Zimmermann, J.P. Hill, D. Gibbs, J.C. Woicik, I. Koyama, Y. Murakami, Phys. Rev. Lett. **85**, 4349 (2000)

32. M. Noguchi, A. Nakazawa, S. Oka, T. Arima, Y. Wakabayashi, H. Nakao, Y. Murakami, Phys. Rev. B **62**, R9271 (2000)
33. K. Ohwada, Y. Fujii, Y. Katsuki, J. Muraoka, H. Nakao, Y. Murakami, H. Sawa, E. Ninomiya, M. Isobe, Y. Ueda, Phys. Rev. Lett. **94**, 106401 (2005)
34. K. Ohwada, Y. Fujii, J. Muraoka, H. Nakao, Y. Murakami, Y. Noda, H. Ohsumi, N. Ikeda, T. Shobu, M. Isobe, Y. Ueda, Phys. Rev. B **76**, 094113 (2007)
35. D. Bizen, N. Shirane, T. Murata, H. Nakao, Y. Murakami, J. Fujioka, T. Yasue, S. Miyasaka, Y. Tokura, J. Phys. Conf. Ser. **150**, 042010 (2009)
36. H. Nakao, D. Bizen, N. Shirane, K. Ikeuchi, Y. Murakami, J. Fujioka, T. Yasue, S. Miyasaka, Y. Tokura, Diam. Light Source Proc. **1**, e115 (2010)
37. R. Fukuta, S. Miyasaka, K. Hemmi, S. Tajima, D. Kawana, K. Ikeuchi, Y. Yamasaki, A. Nakao, H. Nakao, Y. Murakami, K. Iwasa, Phys. Rev. B **84**, 140409 (2011)
38. K. Takubo, T. Kanzaki, Y. Yamasaki, H. Nakao, Y. Murakami, T. Oguchi, T. Katsufuji, Phys. Rev. B **86**, 085141 (2012)
39. T. Akao, Y. Azuma, M. Usuda, Y. Nishihata, J. Mizuki, N. Hamada, N. Hayashi, T. Terashima, M. Takano, Phys. Rev. Lett. **91**, 156405 (2003)
40. N. Ikeda, H. Ohsumi, K. Ohwada, K. Ishii, T. Inami, K. Kakurai, Y. Murakami, K. Yoshii, S. Mori, Y. Horibe, H. Kitô, Nature **436**, 1136 (2005)
41. T. Arima, J.-H. Jung, M. Matsubara, M. Kubota, J.-P. He, Y. Kaneko, Y. Tokura, J. Phys. Soc. Jpn. **74**, 1419 (2005)
42. E. Nazarenko, J.E. Lorenzo, Y. Joly, J.L. Hodeau, D. Mannix, C. Marin, Phys. Rev. Lett. **97**, 056403 (2006)
43. J.E. Lorenzo, C. Mazzoli, N. Jaouen, C. Detlefs, D. Mannix, S. Grenier, Y. Joly, C. Marin, Phys. Rev. Lett. **101**, 226401 (2008)
44. A.M. Mulders, S.M. Lawrence, U. Staub, M. Garcia-Fernandez, V. Scagnoli, C. Mazzoli, E. Pomjakushina, K. Conder, Y. Wang, Phys. Rev. Lett. **103**, 077602 (2009)
45. U. Staub, C. Piamonteze, M. Garganourakis, S.P. Collins, S.M. Koohpayeh, D. Fort, S.W. Lovesey, Phys. Rev. B **85**, 144421 (2012)
46. A. Rodríguez-Fernández, J.A. Blanco, S.W. Lavesey, V. Scgnoli, U. Staub, H.C. Walker, D.K. Shukla, J. Strempfer, Phys. Rev. B **88**, 094437 (2013)
47. K. Horigane, H. Nakao, Y. Kousaka, T. Murata, Y. Noda, Y. Murakami, J. Akimitsu, J. Phys. Soc. Jpn. **77**, 044601 (2008)
48. H. Nakao, T. Murata, D. Bizen, Y. Murakami, K. Ohoyama, K. Yamada, S. Ishiwata, W. Kobayashi, I. Terasaki, J. Phys. Soc. Jpn. **80**, 023711 (2011)
49. J. Fujioka, Y. Yamasaki, H. Nakao, R. Kumai, Y. Murakami, M. Nakamura, M. Kawasaki, Y. Tokura, Phys. Rev. Lett. **111**, 027206 (2013)
50. J. Fujioka, Y. Yamasaki, A. Doi, H. Nakao, R. Kumai, Y. Murakami, M. Nakamura, M. Kawasaki, T. Arima, Y. Tokura, Phys. Rev. B **92**, 195115 (2015)
51. U. Staub, G.I. Meijer, F. Fauth, R. Allenspach, J.G. Bednorz, J. Karpinski, S.M. Kazakov, L. Paolasini, F. d'Acapito, Phys. Rev. Lett. **88**, 126402 (2002)
52. V. Scagnoli, U. Staub, M. Janousch, A.M. Mulders, M. Shi, G.I. Meijer, S. Rosenkranz, S.B. Wilkins, L. Paolasini, J. Karpinski, S.M. Kazakov, S.W. Lovesey, Phys. Rev. B **72**, 155111 (2005)
53. Y. Lu, A. Frano, M. Bluschke, M. Hepting, S. Macke, J. Strempfer, P. Wochner, G. Cristiani, G. Logvenov, H.-U. Habermeier, M.W. Haverkort, B. Keimer, E. Benckiser, Phys. Rev. B **93**, 165121 (2016)
54. L. Paolasini, R. Caciuffo, A. Sollier, P. Ghigna, M. Altarelli, Phys. Rev. Lett. **88**, 106403 (2002)
55. R. Caciuffo, L. Paolasini, A. Sollier, P. Ghigna, E. Pavarini, J. van den Brink, M. Altarelli, Phys. Rev. B **65**, 174425 (2002)
56. N. Tatami, Y. Ando, S. Niioka, H. Kira, M. Onodera, H. Nakao, K. Iwasa, Y. Murakami, T. Kakiuchi, Y. Wakabayashi, H. Sawa, S. Itoh, J. Magn. Magn. Mater. **310**, 787 (2007)
57. D.T. Cromer, D. Liberman, J. Chem. Phys. **53**, 1891 (1970)
58. D.T. Cromer, D. Liberman, Acta Crystallogr. Sect. A **37**, 267 (1981)

59. S. Sasaki, KEK Peport No. 88-14 (1989)
60. J.O. Cross, M. Newville, J.J. Rehr, L.B. Sorensen, C.E. Bouldin, G. Watson, T. Gouder, G.H. Lander, M.I. Bell, Phys. Rev. B **58**, 11215 (1998), http://cars.uchicago.edu/~newville/dafs/diffkk/
61. O. Šipr, A. Šimůnek, S. Bocharov, T. Kirchner, G. Dräger, Phys. Rev. B **60**, 14115 (1999)
62. J.P. Hill, D.F. Mcmorrw, Acta Crystallogr. Sect. A **52**, 236 (1996)
63. S. Ishihara, S. Maekawa, Phys. Rev. Lett. **80**, 3799 (1998)
64. S. Ishihara, S. Maekawa, Phys. Rev. B **58**, 13442 (1998)
65. S. Ishihara, S. Maekawa, Phys. Rev. B **62**, 5690 (2000)
66. I.S. Elfimov, V.I. Anisimov, G.A. Sawatzky, Phys. Rev. Lett. **82**, 4264 (1999)
67. M. Benfatto, Y. Joly, C.R. Natoli, Phys. Rev. Lett. **83**, 636 (1999)
68. M. Takahashi, J. Igarashi, P. Fulide, J. Phys. Soc. Jpn. **68**, 2530 (1999)
69. Y. Murakami, H. Nakao, T. Matsumura, H. Ohsumi, J. Magn. Magn. Mater. **310**, 895 (2007)
70. T. Mizokawa, A. Fujimori, Phys. Rev. B **54**, 5368 (1996)
71. T. Mizokawa, D.I. Khomskii, G.A. Sawatzky, Phys. Rev. B **60**, 7309 (1999)
72. H. Sawada, N. Hamada, K. Terakura, Phys. B **237–238**, 46 (1997)
73. H. Ichikawa, J. Akimitsu, M. Nishi, K. Kakurai, Phys. B **281–282**, 428 (2000)
74. J. Akimitsu, H. Ichikawa, N. Eguchi, T. Miyano, M. Nishi, K. Kakurai, J. Phys. Soc. Jpn. **70**, 3475 (2001)
75. M. Ito, M. Tsuchiya, H. Tanaka, K. Motoya, J. Phys. Soc. Jpn. **68**, 2783 (1999)
76. D.A. Maclean, H.-N. Ng, J.E. Greedan, J. Solid State Chem. **30**, 35 (1979)
77. S. Ishihara, T. Hatakeyama, S. Maekawa, Phys. Rev. B **65**, 064442 (2002)
78. M. Takahashi, J. Igarashi, Phys. Rev. B **64**, 075110 (2001)
79. M. Fabrizio, M. Altarelli, M. Benfatto, Phys. Rev. Lett. **80**, 3400 (1998)
80. Y. Taguchi, Y. Tokura, T. Arima, F. Inaba, Phys. Rev. B **48**, 511 (1993)
81. K. Kumagai, T. Suzuki, Y. Taguchi, Y. Okada, Y. Fujishima, Y. Tokura, Phys. Rev. B **48**, 7636 (1993)
82. Y. Tokura, Y. Taguchi, Y. Moritomo, K. Kumagai, T. Suzuki, Y. Iye, Phys. Rev. B **48**, 14063 (1993)
83. F. Iga, T. Nishiguchi, Y. Nishihara, Phys. B **206–207**, 859 (1995)
84. F. Iga, T. Naka, T. Matsumoto, N. Shirakawa, K. Murata, Y. Nishihara, Phys. B **223–224**, 526 (1996)
85. P. Benedetti, J. Brink, E. Pavarini, A. Vigliante, P. Wochner, Phys. Rev. B **63**, 060408(R) (2001)
86. J. Rodríguez-Carvajal, M. Hennion, F. Moussa, A.H. Moudden, Phys. Rev. B **57**, 3189(R) (1998)
87. T. Koida, M. Lippmaa, T. Fukumura, K. Itaka, Y. Matsumoto, M. Kawasaki, H. Koinuma, Phys. Rev. B **66**, 144418 (2002)
88. H. Yamada, P.-H. Xiang, A. Sawa, Phys. Rev. B **81**, 014410 (2010)
89. M. Izumi, T. Manako, Y. Konishi, M. Kawasaki, Y. Tokura, Phys. Rev. B **61**, 12187 (2000)
90. K. Ohwada, K. Ishii, T. Inami, Y. Murakami, T. Shobu, H. Ohsumi, N. Ikeda, Y. Ohishi, Phys. Rev. B **72**, 014123 (2005)
91. K. Ohwada, Y. Fujii, N. Takesuke, M. Isobe, Y. Ueda, H. Nakao, Y. Wakabayashi, Y. Murakami, K. Ito, Y. Amemiya, H. Fujihisa, K. Aoki, T. Shoubu, Y. Noda, N. Ikeda, Phys. Rev. Lett. **87**, 086402 (2001)
92. K. Asai, O. Yokokura, N. Nishimori, H. Chou, J.M. Tranquada, G. Shirane, S. Higuchi, Y. Okajima, K. Kohn, Phys. Rev. B **50**, 3025 (1994)
93. T. Saitoh, T. Mizokawa, A. Fujimori, M. Abbate, Y. Takeda, M. Takano, Phys. Rev. B **55**, 4257 (1997)
94. G. Maris, Y. Ren, V. Volotchaev, C. Zobel, T. Lorenz, T.T.M. Palstra, Phys. Rev. B **67**, 224423 (2003)
95. M. Itoh, M. Sugihara, I. Natori, K. Motoyama, J. Phys. Soc. Jpn. **64**, 3967 (1995)
96. S. Noguchi, S. Kawamata, K. Okuda, H. Nogiri, M. Motokawa, Phys. Rev. B **66**, 094404 (2002)

97. M.W. Haverkort, Z. Hu, J.C. Cezar, T. Burnus, H. Hartmann, M. Reuther, C. Zobel, T. Lorenz, A. Tanaka, N.B. Brookes, H.H. Hsieh, H.-J. Lin, C.T. Chen, L.H. Tjeng, Phys. Rev. Lett. **97**, 176405 (2006)
98. W. Kobayashi, S. Ishiwata, I. Terasaki, M. Takano, I. Grigoraviciute, H. Yamaguchi, M. Karppinen, Phys. Rev. B **72**, 104408 (2005)
99. W. Kobayashi, S. Yoshida, I. Terasaki, J. Phys. Soc. Jpn. **75**, 103702 (2006)
100. W. Kobayashi, I. Terasaki, AIP Conf. Proc. **850**, 1223 (2006)
101. S. Ishiwata, W. Kobayashi, I. Terasaki, K. Kato, M. Takata, Phys. Rev. B **75**, 220406 (2007)

http://www.springer.com/978-3-662-53225-6

Resonant X-Ray Scattering in Correlated Systems
Murakami, Y.; Ishihara, S. (Eds.)
2017, VII, 241 p. 151 illus., 25 illus. in color., Hardcover
ISBN: 978-3-662-53225-6